Aggravated surface O₃ pollution primarily driven by meteorological variation in China during the 2020 COVID-19 pandemic lockdown period

Zhendong Lu[1*], Jun Wang[1,2*], Yi Wang[2,3], Daven K. Henze[4], Xi Chen[2], Tong Sha[2,5], Kang Sun[6,7]

[1]*Interdisciplinary Graduate Program in Informatics, The University of Iowa, Iowa City, IA, United States*

[2]*Department of Chemical and Biochemical Engineering, Center for Global and Regional Environmental Research and Iowa Technology Institute, The University of Iowa, Iowa City, IA, United States*

[3]*Now at Hubei Key Laboratory of Regional Ecology and Environmental Change, School of Geography and Information Engineering, China University of Geosciences, Wuhan, China*

[4]*Department of Mechanical Engineering, University of Colorado, Boulder, CO, United States*

[5]*Now at School of Environmental Science and Engineering, Shaanxi University of Science and Technology, Xi'an, China*

[6]*Department of Civil, Structural and Environmental Engineering, University at Buffalo, Buffalo, NY, United States*

[7]*Research and Education in Energy, Environment and Water Institute, University at Buffalo, Buffalo, NY, United States*

*Correspondence to: Jun Wang (jun-wang-1@uiowa.edu) and Zhendong Lu (zhendong-lu@uiowa.edu)

Submitted: November 2023

First Revised Submission: April 2024

Second Revised Submission: May 2024

Abstract

Due to the lockdown during the COVID-19 pandemic in China from late January to early April in 2020, a significant reduction of primary air pollutants, as compared to the same time period in 2019, has been identified by satellite and ground observations. However, this reduction is in contrast with the increase of surface O_3 concentration in many parts of China during the same period from 2019 to 2020. The reasons for this contrast are studied here from two perspectives: emission changes and inter-annual meteorological variations. Based on top-down constraints of NOx emissions from TROPOMI measurements and GEOS-Chem model simulations, our analysis reveals that NOx and volatile organic compound (VOC) emission reductions as well as meteorological variations lead to 8%, -3%, and 1% changes in O_3 over North China, respectively. In South China, however, we find that meteorological variations cause ~30% increases in O_3, which is much larger than -1% and 2% changes due to VOC and NOx emission reductions, respectively, and the overall O_3 increase in the simulations is consistent with the surface observations. The higher temperature associated with increase of solar radiation and declined relative humidity are the main reasons that lead to the surface O_3 increase in South China. Collectively, inter-annual meteorological variations have a larger impact than emission reductions on the aggravated surface O_3 pollution in China during the lockdown period of COVID-19 pandemic.

1. Introduction

Surface ozone (O_3), an important air pollutant that is harmful to human health (Jerrett et al., 2009) and stomatal conductance of green vegetations (Gong et al., 2020), is produced by photochemical reactions of nitrogen oxides (NOx) and volatile organic compounds (VOC) (Liu et al., 1987; Sillman et al., 1990). In addition to emissions, meteorological conditions, such as temperature, solar radiation and relative humidity, also have large impacts on surface O_3 formation (Lu et al., 2019).

Ground observations show that surface O_3 increased dramatically during the COVID-19 lockdown period in China by around 40% on average (Tong et al., 2023) and even larger than 100% (Shi and Brasseur, 2020; Liu et al., 2021) depending on the time period and region. The reduction of economic activities during the lockdown period led to a significant decrease of several primary air pollutants emissions. The NO_2 vertical column density (VCD) from satellite measurements and

60   surface NO_2 concentration from ground measurements were reduced by 40% - 60% in China

61   during the lockdown period (Bauwens et al., 2020; Shi and Brasseur, 2020; Liu et al., 2020a; Zhang

62   et al., 2020). A lower but discernible reduction of sulfur dioxide (SO_2), carbon monoxide (CO),

63   and formaldehyde (HCHO) have also been identified by satellite or ground-based observations in

64   China (Shi and Brasseur, 2020; Levelt et al., 2022; Ghahremanloo et al., 2021). However, during

65   this period surface O_3 concentrations increased, and the respective roles of meteorological factor

66   and emission reduction for the aggravated surface O_3 pollution during the lockdown in China need

67   to be further quantified.

68   This study provides a quantitative analysis of the causes for the unexpectedly aggravated

69   surface O_3 pollution in China during the lockdown period of the pandemic from two perspectives

70   using GEOS-Chem model. One is anthropogenic emission reduction of NOx and VOC in response

71   to the lockdown possibly under a VOC-limiting chemical regime of surface O_3 production (Guo

72   et al., 2023), while the other is the impact of natural variability of meteorological conditions.

73   Previous studies have reported the enhanced surface O_3 due to NOx emission decline during the

74   lockdown period in North China using chemical transport model (CTM) simulations without

75   controlling for the impacts of meteorological variability (Zhang et al., 2021; Huang et al., 2020;

76   Miyazaki et al., 2020). Other studies quantified or excluded the meteorological impacts on the

77   surface O_3 using statistical analysis instead of CTM that account for the physical and chemical

78   processes (Venter et al., 2020; Bi et al., 2022; Tong et al., 2023). Although a few studies have

79   investigated the contributions from both emission reduction and meteorological variability to

80   surface O_3 increase using CTMs, most of their results have uncertainties due to the limitations of

81   their analysis. For example, some of them keep the emissions unchanged (Zhao et al., 2020) or

82   assume an arbitrarily uniform emission reduction instead of constraining the emission based on

83   observations (Le et al., 2020; Liu et al., 2021). In cases where the emissions were constrained by

84   the observations, the focus was limited to several cities in China (Liu et al., 2020b). Furthermore,

85   in the past studies, the surface O_3 increase during the lockdown period of 2-4 weeks is quantified

86   in reference to the time period right before the lockdown instead of the same period in previous

87   years; such comparisons by design cannot exclude the possibility that the seasonal variation of

88   meteorology from early January to early April may have dominated the cause for the surface O_3

89   increase. A comprehensive analysis of the contributions from emission reductions and

90 meteorological variations to the surface O_3 increase during the first round of the lockdown period

91 with respect to the same time period in previous years in China is therefore overdue.

92   Here, we apply a top-down method to update NOx and VOC emission in February and

93 March in 2020 based on the TROPOMI NO_2 and formaldehyde (HCHO) product. A set of GEOS-

94 Chem model simulations with NOx and VOC emissions and meteorological fields in different time

95 periods are then conducted. Based on the difference in surface O_3 concentration in different

96 modeling sensitivity experiments, we quantitatively assess the respective roles of emission and

97 meteorology in regulating surface O_3 concentration in continental China. The ground observations

98 of surface O_3 and NO_2 concentration are compared with the model simulations to verify our

99 analysis. Section 2 introduces the satellite and ground-based measurements, NOx emission update

100 scheme, and the configurations of GEOS-Chem simulation experiments. Section 3 provides an

101 evaluation of the constrained NOx emission and surface O_3 simulations. The analysis of the

102 mechanism of the aggravated surface O_3 pollution is presented in Section 4, followed by the

103 summary and conclusions in Section 5.

104

105 **2. Datasets and Methods**

106 **2.1 TROPOMI NO_2 and HCHO product**

107   We used tropospheric NO_2 and HCHO level 2 VCD product provided by the Tropospheric

108 Monitoring Instrument (TROPOMI) onboard the Sentinel-5 Precursor (S5P) satellite (Veefkind et

109 al., 2012). S5P is a sun-synchronous polar orbit satellite launched on 13 October 2017, which

110 covers the near-global domain in a single day. TROPOMI provides NO_2 and HCHO retrievals at

111 an approximately 7 km x 3.5 km spatial resolution (5.5km x 3.5 km since 6 August 2019) from the

112 ascending orbit with an equatorial crossing time of ~13:30 local time (Van Geffen et al., 2020; De

113 Smedt et al., 2018). The datasets were obtained from the NASA Goddard Earth Sciences Data and

114 Information Services Center (https://daac.gsfc.nasa.gov). A quality control procedure similar to

115 Bauwens et al. (2020) but with slightly stricter criteria is adopted for TROPOMI NO_2 and HCHO

116 data. The TROPOMI retrievals under one or more than one of the following conditions are

117 screened out for data quality control. (1) Quality assurance value is no larger than 0.5; (2) cloud

118 radiance fraction within NO_2 or HCHO retrieval window is larger than 0.3; (3) solar zenith angle

119 is larger than 70°; and (4) viewing zenith angle is larger than 70°.

120

2.2 Ground O_3 and NO_2 measurements

Surface measurements of O_3 and NO_2 were collected from ~1600 operational air quality monitoring stations over the mainland China managed by the China National Environmental Monitoring Center (http://www.cnemc.cn/en/). We calculated daily maximum 8-hour average (MDA8) O_3 concentration from hourly in situ measurements. Surface O_3 are measured by ultraviolet photometric method and Indigo disulfonate spectrophotometry, following the national environmental standards of HJ 590-2010 and HJ 504-2009. Surface NO_2 concentrations are measured by the chemiluminescence method (Zhang and Cao, 2015) that quantifies the NO_2 concentrations by measuring the NO decomposed from NO_2, which can cause a positive bias in the NO_2 measurements (Steinbacher et al., 2007) because NOz (compounds produced from the atmospheric oxidation of NOx) can also be decomposed to NO. The true NO_2 concentrations only account for 43%-76% and 70%-83% of measured values for rural and urban sites (Steinbacher et al., 2007). Following Wang et al. (2020b), we also applied a correction factor but with a lower value of 0.75 to the measured NO_2, considering that we included both rural and urban sites. The sampling ports are placed at 3 to 15 meters above the ground following the national environmental monitoring method standard HJ 664-2013. The measured data are reported in the unit of $\mu g\ m^{-3}$ under standard temperature (273.15 K) and pressure (101.325 kPa) according to national environmental standards GB 3095-2012.

2.3 GEOS-Chem model and its adjoint

The global 3-D chemical transport model GEOS-Chem (Bey et al., 2001) version 12.7.2 is used here. We apply the nested-grid version of GEOS-Chem (Chen et al., 2009; Wang et al., 2004) with the horizontal resolution of $0.25°\times0.3125°$ and 47 vertical hybrid-sigma levels over East Asia (70°E-140°E, 15°N-55°N). The boundary conditions are obtained from the $2°\times2.5°$ global simulation. The model is driven by the GEOS-FP meteorological field provided by NASA Global Modeling and Assimilation Office (GMAO). A detailed O_3-NOx-hydrocarbon chemistry (Mao et al., 2010; Mao et al., 2013; Travis et al., 2016) is included in the GEOS-Chem model. The altitude of the surface O_3 output from GEOS-Chem is specified at 9 meters above the ground to match the in-situ measurements (Travis et al., 2017; Zhang et al., 2012). Through our sensitivity test using GEOS-Chem, the variation of surface O_3 from 3 to 9 meters above the surface is generally less than 0.723 ppb (75th percentile), and the median bias is 0.283 ppb. Travis et al. (2017) reported

152   from 60 m to 10 m above the ground, the MDA8 O_3 could decrease by ~3 ppb. Therefore, when

153   comparing GEOS-Chem surface O3 with in-situ measurements, the differences caused by

154   inconsistent reported altitudes (9 m versus 3-15 m) can be ignored.

155   The global anthropogenic emission used in GEOS-Chem model is the Community

156   Emissions Data System (CEDS) inventory (Hoesly et al., 2018), which is replaced by the MIX

157   inventory (Li et al., 2017) over the Asian region. Biogenic emissions for VOCs follows the Model

158   of Emissions of Gases and Aerosols from Nature (MEGAN) inventory (Guenther et al., 2012).

159   Natural NOx emissions includes biomass burning from GFED4 inventory (Van Der Werf et al.,

160   2017), soil NOx emissions (Hudman et al., 2012) and lightning sources (Murray et al., 2012; Ott

161   et al., 2010).

162   The adjoint of the GEOS-Chem model (Henze et al., 2007; Henze et al., 2009) is a

163   component of the 4D-Var inversion method that can efficiently optimize spatially disaggregated

164   aerosol and gas emissions. This is done through iterative minimization of a cost function using the

165   model adjoint to calculate the gradient of the cost function with respect to a large number of model

166   parameters (such as anthropogenic NOx emissions in each grid box) simultaneously. The cost

167   function is the sum of the error weighted difference between forward model outputs and

168   observations and the divergence of posterior model parameters from the prior estimate (Section

169   2.4). We developed and validated the observation operator for TROPOMI NO_2 in the GEOS-Chem

170   adjoint model version 35n similar to Wang et al. (2020a) and used it to optimize the anthropogenic

171   NOx emission during the lockdown period in China. The monthly NOx emission optimization is

172   implemented using the 4D-Var method with GEOS-Chem adjoint at the nested grid with the

173   resolution of 0.25°×0.3125° via assimilating the daily TROPOMI NO_2 measurements. The prior

174   anthropogenic NOx emission used in the GEOS-Chem adjoint is HTAP version 2 (Janssens-

175   Maenhout et al., 2015), which is equivalent to the MIX inventory in East Asia (Li et al., 2017).

176

177   **2.4 NOx and VOC emission updates**

178   Two approaches are used to update the emissions during the lockdown period in 2020. The

179   first is a simple mass balance approach (Leue et al., 2001; Martin et al., 2003; Vinken et al., 2014)

180   for updating the NOx emission by assuming a constant NOx lifetime and NOx/NO_2 ratio. In the

181   period from 2010 to 2019, the anthropogenic NOx emissions have declined significantly as a result

182   of the clean air actions of Chinese government (Zheng et al., 2018). We scale the anthropogenic

NOx emission from year 2010 to 2019 using the spatially gridded ratio of mean TROPOMI tropospheric NO_2 VCD in Feb.-Mar. 2019 to GEOS-Chem simulated NO_2 column with default MIX 2010 emission (Appendix A), to obtain the baseline anthropogenic NOx emission in 2019, which is denoted as MIX 2019. To derive anthropogenic NOx emissions in 2020 in China during the COVID-19 lockdown (MIX 2020), the spatially gridded ratio of mean TROPOMI tropospheric NO_2 VCD in 2020 Feb.-Mar. to that in 2019 Feb.-Mar. is taken as a scaling factor for the updated baseline anthropogenic NOx emission in 2019 (MIX 2019). The two-month mean of TROPOMI NO_2 VCD in 2019 and 2020 are calculated with the physical oversampling procedure (Sun et al., 2018). Scaling factors in regions where mean TROPOMI tropospheric NO_2 VCD in 2019 Feb.-Mar. is less than 0.1 Dobson unit (DU) are set to 1 for emission updates in both 2020 and 2019, assuming that the lockdown only affects the populated areas (that have high NO_2 in 2019).

The second method for updating NOx emission is 4D-Var via the GEOS-Chem adjoint model. The anthropogenic NOx emissions in 2020 lockdown period derived from the GEOS-Chem adjoint is denoted as 2020 Adjoint. Following Wang et al. (2020a), the cost function J for optimizing the NOx emission is defined as

$$J = \frac{1}{2}\sum_{c\in\Omega}[H(\boldsymbol{c}) - \boldsymbol{s}]^{\mathrm{T}}\boldsymbol{S}_{\mathrm{obs}}^{-1}[H(\boldsymbol{c}) - \boldsymbol{s}] + \frac{1}{2}\gamma(\boldsymbol{\sigma} - \boldsymbol{\sigma}_a)^{\mathrm{T}}\boldsymbol{S}_a^{-1}(\boldsymbol{\sigma} - \boldsymbol{\sigma}_a) \tag{1}$$

where $\boldsymbol{s}$ is the tropospheric slant column density of TROPOMI NO_2, which is the product of TROPOMI NO_2 VCD and air mass factor. H is the TROPOMI NO_2 observation operator that maps the modeled NO_2 concentrations $\boldsymbol{c}$ to the observations in time and space and calculates the corresponding slant column density to make an apple-to-apple comparison of the model to TROPOMI. Ω is the spatial and temporal domain where both model simulations and observations are available. $\boldsymbol{\sigma}$ is the scaling factor of anthropogenic NOx emissions to be optimized, and $\boldsymbol{\sigma}_a$ is the prior emission scaling factors, which equals 1. $\boldsymbol{S}_{\mathrm{obs}}$ and $\boldsymbol{S}_a$ are observational and prior error covariance matrices, respectively. γ is the regularization factor that balances the weights of the observational term and prior term. We assumed $\boldsymbol{S}_{\mathrm{obs}}$ to be diagonal following Wang et al. (2020a) with the diagonal values calculated as the square of the standard error of tropospheric NO_2 slant column density from the TROPOMI product. The prior error of the NOx emissions is assumed to be 100%. The spatial correlation of NOx emissions is considered in this study, and the off-diagonal elements of $\boldsymbol{S}_a$ are computed by assuming an exponentially decaying error correlation with a fixed

212 decaying distance of 150 km following Qu et al. (2017). The γ value was determined as 500 via

213 the total error minimization and L-curve test (Henze et al., 2009; Qu et al., 2017).

214   We developed the observation operator for TROPOMI NO_2 product in the GEOS-Chem

215 adjoint model with GEOS-Chem NO_2 vertical profiles and TROPOMI NO_2 averaging kernel

216 applied to minimize the discrepancies between the assumptions in TROPOMI NO_2 retrieval and

217 GEOS-Chem model simulation. See Appendix B for additional details. The observation operator

218 has been validated using the finite difference method (Appendix C).

219   For anthropogenic VOC emissions update, we only applied the mass balance method based

220 on the TROPOMI HCHO data. The default anthropogenic VOC emissions used in the GEOS-

221 Chem is also MIX 2010 (Li et al., 2017). We ignore the change of anthropogenic VOC emissions

222 from 2010 to 2019 (Appendix D). The baseline VOC emission in 2019 (MIX 2019) is identical to

223 that of MIX 2010. The updated anthropogenic VOC emissions during the lockdown period is

224 denoted as MIX 2020. HCHO is one species of VOC and may not be able to represent other VOC

225 species. Different from NOx, biogenic sources, meteorological impacts, and large retrieval

226 uncertainty of HCHO due to its low optical depth prevent accurately quantifying the emission

227 decline due to lockdown from satellite retrievals (Levelt et al., 2022). Vigouroux et al. (2020)

228 reported that TROPOMI HCHO tends to be overestimated by ~26% for HCHO column lower than

229 2.5×10^{15} molecules cm^{-2} and underestimated by ~31% for HCHO column higher than 8.0×10^{15}

230 molecules cm^{-2}. To optimize the signal, we spatially aggregate the ratio of TROPOMI HCHO in

231 2020 Feb.-Mar. to that in 2019 Feb.-Mar. to the resolution of 0.5°, which are used as the scaling

232 factors for updating the anthropogenic VOC emissions during the lockdown period. The

233 aggregation is based on the oversampling of TROPOMI HCHO at 0.01° resolution, and the ratio

234 is computed as the mean of the lowest 25th percentile of all ratios at 0.01° resolution in each

235 0.5°×0.5° grid box, which ensures that only statistically significant changes are considered. We

236 assumed the change of anthropogenic VOC emissions over sparsely populated areas (TROPOMI

237 NO_2 in 2019 Feb.-Mar. less than 0.1 DU) is insignificant and assigned the ratio values as one. To

238 further evaluate the uncertainties associated with this approach, we also conducted sensitivity

239 study by using different threshold in the aggregation.

240   We assess the results from model experiments (as described in Section 2.5) adopting the

241 updated NOx emission by comparing mean tropospheric NO_2 VCD from GEOS-Chem and from

242 TROPOMI observations in Feb.-Mar. of 2019 and 2020. The averaging kernel of TROPOMI NO_2

243 is applied to modeled NO_2 column for this comparison, following Sha et al. (2021). Further
244 quantitative evaluation of the model results also used the TROPOMI measurements of HCHO and
245 surface observation of O_3 and NO_2.

246

247 **2.5 GEOS-Chem model experiments**

248   A series of sensitivity experiments is conducted over China with different NOx and VOC
249 emissions and GEOS-FP meteorological fields in different years using GEOS-Chem (v12.7.2)
250 model. All simulations are conducted from Jan. 15 to Mar. 31. The 17 days before Feb. 1 are used
251 for spin up, and the model output for Feb. and Mar. are used for the analysis. The configurations
252 of different simulations are listed in Table 1.

253

254 **Table 1.** Configurations of model sensitivity experiments.

Experiments	Abbreviation	Meteorology	NOx Emission	VOC Emission
Baseline (2019)	2019B	GEOS-FP 2019	MIX 2019	MIX 2019
2020 Default	2020D	GEOS-FP 2020	MIX 2019	MIX 2019
2020 NOx	2020N	GEOS-FP 2020	MIX 2020	MIX 2019
2020 VOC	2020V	GEOS-FP 2020	MIX 2019	MIX 2020
2020 Lockdown	2020L	GEOS-FP 2020	MIX 2020	MIX 2020
2020 Adjoint	2020A	GEOS-FP 2020	Adjoint 2020	MIX 2020

255

256   We use the following equations to quantify the contributions from NOx and VOC emission
257 reduction due to COVID-19 and meteorological variation to the increase of surface O_3.

258
$$\Delta O_3^{NOx} = \frac{O_3^{2020A} - O_3^{2020V}}{O_3^{2019B}} \times 100\% \tag{2}$$

259
$$\Delta O_3^{VOC} = \frac{O_3^{2020L} - O_3^{2020N}}{O_3^{2019B}} \times 100\% \tag{3}$$

260
$$\Delta O_3^{ems} = \frac{O_3^{2020A} - O_3^{2020D}}{O_3^{2019B}} \times 100\% \tag{4}$$

261
$$\Delta O_3^{met} = \frac{O_3^{2020D} - O_3^{2019B}}{O_3^{2019B}} \times 100\% \tag{5}$$

262 Where ΔO_3^{NOx}, ΔO_3^{VOC} and ΔO_3^{ems} are the relative differences in surface O₃ concentration caused

263 by emission decline of NOx, VOC, and both NOx and VOC resulting from COVID-19. ΔO_3^{met}

264 represents the relative contribution to the surface O₃ change from the meteorological variation

265 between 2 years. O_3^{2019B}, O_3^{2020D}, O_3^{2020N}, O_3^{2020V}, O_3^{2020L} and O_3^{2020A} are mean MDA8 surface

266 O₃ concentration simulated by modeling experiments Baseline (2019), 2020 Default, 2020 NOx,

267 2020 VOC, 2020 Lockdown and 2020 Adjoint, respectively (Table 1).

268   The difference in simulated surface O₃ between 2020 and 2019, is the result of both

269 emission reductions and meteorological variations and is denoted as ΔO_3^{all}. It is calculated as

270 follows and is evaluated against the observed relative difference of mean MDA8 O₃ in Feb. to Mar.

271 between 2019 and 2020 at all ground sites:

272
$$\Delta O_3^{all} = \frac{O_3^{2020A} - O_3^{2019B}}{O_3^{2019B}} \times 100\% \tag{6}$$

273

3. Results of model development, emissions, and validation

3.1 Changes of NOx and VOC emissions during COVID

276   We updated the anthropogenic NOx emissions during the COVID lockdown using both

277 4D-Var and mass balance methods (Fig. 1 and 2). The NOx emissions from the 4D-Var inversion

278 share a similar spatial pattern and magnitude with those found using the mass balance method (Fig.

279 1). However, the NOx emissions from the 4D-Var inversion are lower overall than those from the

280 mass balance method over North China by ~10% and larger over central China by ~40%. Fig. 2(a-

281 b) shows that the 4D-Var NOx emission reduction is more severe over urban regions and displays

282 a smoother spatial pattern than that from the mass balance approach, which is caused by the

283 arbitrary cut off with 0.1 DU of NO₂ VCD in the latter. Furthermore, the 4D-Var inversion

284 captured the NOx emission decline in Northeast China where the mass balance approach did not

285 because of the low NO₂ VCD. During Feb.-Mar. 2020, the anthropogenic NOx emissions in East

286 China decreased by ~30% compared to those in the same period in 2019.

287   We also scale the anthropogenic VOC emissions based on the TROPOMI HCHO data (Fig.

288 2(c)). The VOC emissions decrease by ~20%-30% in East and South Asia. The anthropogenic

289 VOC emission changes in sparsely populated areas over Northwest China are neglected.

290 TROPOMI HCHO data cannot distinguish the anthropogenic emissions from biogenic and

291 biomass burning sources for the Indochinese Peninsula in Southeast Asia because of the dense

292 vegetation in this region. However, this study investigated the O₃ pollution in China, the Southeast

293 Asia with the dense vegetation is out of our study domain. The impact of VOC emission bias in

294 Southeast Asia on the surface O₃ pollution in China is negligible considering the lifetime of

295 biogenic VOC is generally short (Atkinson, 2000). For the populated urban regions in China,

296 where the surface O₃ pollution exerts more significant health impacts, the anthropogenic source

297 dominates the VOC emissions (Williams and Koppmann, 2007).

298
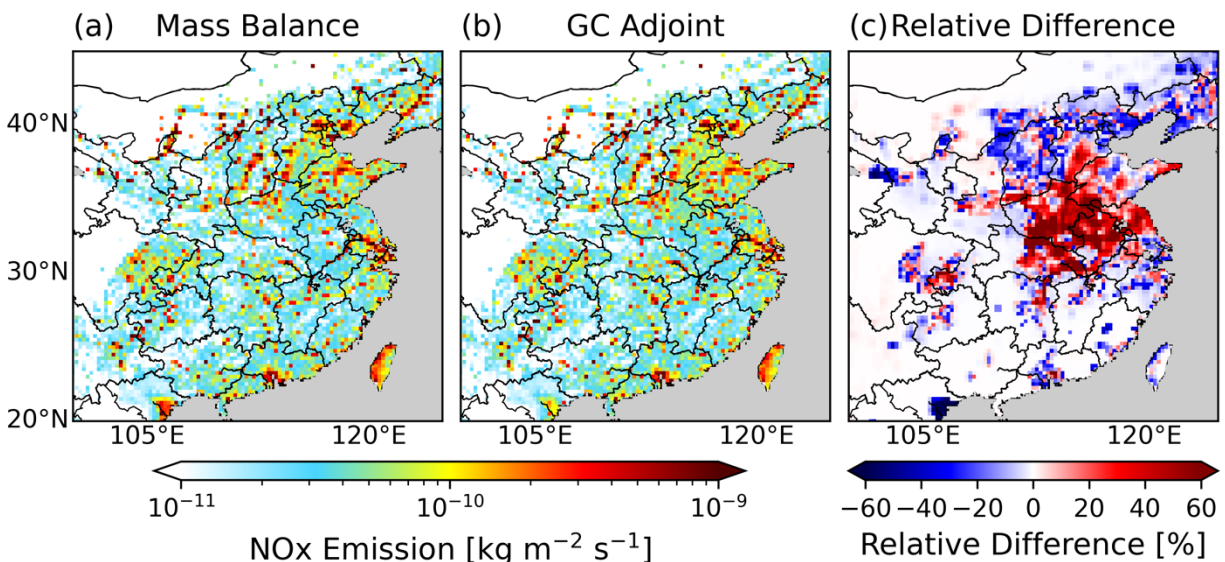
299 **Figure 1.** Updated anthropogenic NOx emission during Feb.-Mar. 2020 from (a) mass balance

300 method, (b) 4D-Var method and (c) their relative difference. The relative difference is calculated

301 as dividing the difference of (b) minus (a) by (a).

302

303
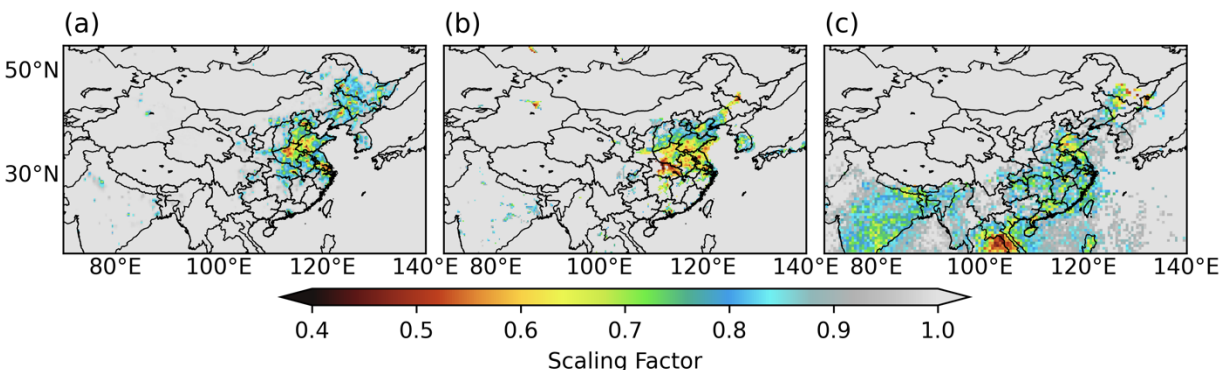
304 **Figure 2.** Scaling factors for anthropogenic NOx emission in Feb.-Mar. from 2019 to 2020 as

305 derived from (a) 4D-Var, (b) mass balance. Scaling factors for anthropogenic VOC emissions from

306 the mass balance are in (c).

307

3.2 Validation of NO$_2$ simulations

309   We further assess our updated anthropogenic NOx emissions by comparing the NO$_2$ VCD

310   from TROPOMI with that from GEOS-Chem with the anthropogenic NOx emissions before and

311   after the scaling (Fig. 3 and 4). Before updating the NOx emissions, the 2020 Default (Fig. 3(b))

312   simulation significantly overestimates the NO$_2$ VCD compared to the TROPOMI NO$_2$

313   observations (Fig. 3(a)). With the NOx emissions updated, the simulations 2020 NOx (Fig. 3(c))

314   and 2020 Adjoint (Fig. 3(d)) exhibit a much better agreement with TROPOMI NO$_2$ observation

315   than 2020 Default. However, Fig. 3(c) shows the GEOS-Chem simulation with the NOx emissions

316   from mass balance approach overestimated the NO$_2$ VCD over Beijing and southwest of Hebei

317   Province (pink and black circles in Fig.3) compared with TROPOMI data. The reason is that

318   scaling factors are applied only to anthropogenic NOx emissions, not total NOx emissions, so it is

319   expected that the model may still overestimate the NO$_2$ column after scaling part of the total NOx

320   emission. With the anthropogenic NOx emissions optimized by the 4D-Var method, the

321   overestimation of NO$_2$ VCD over Beijing and southwest of Hebei Province (pink and black circles

322   in Fig. 3) is mitigated compared with the NOx emissions from mass balance approach.

323   Fig. 4 further displays the statistics for the comparison between the TROPOMI NO$_2$ and

324   GEOS-Chem simulations via the scatterplot. The Baseline (2019) simulation captures the

325   magnitude of NO$_2$ VCD observations in 2019 well (Fig. 4(a)). The root-mean-square-error (RMSE)

326   and mean bias error (MBE) for the simulation with 2020 NOx emission derived from mass balance

327   method (Fig. 4(b)) decreased by 0.050 DU and 0.057 DU as compared to the 2020 Default (Fig.

328   4(c)). Compared with the result from GEOS-Chem simulation 2020 NOx, emissions from 2020

329   Adjoint (Fig. 4(d)) further led to the reduction of the MBE of the NO$_2$ VCD by 0.006 DU and

330   improve the correlation coefficient by 0.003. The significant overestimation of several pixels with

331   TROPOMI NO$_2$ VCD larger than 0.4 DU by the simulation 2020 NOx is also mitigated by 2020

332   Adjoint. The MBE between GEOS-Chem and TROPOMI for Baseline (2019), 2020 NOx and

333   2020 Adjoint are -0.004, 0.015 and 0.009 DU, respectively. The corresponding relative bias are

334   1.9%, 10% and 6.0%, which are all less than the relative uncertainty of ~30% for TROPOMI

335   tropospheric NO$_2$ VCD over East China (Van Geffen et al., 2022). The improved agreement

336   between the simulation with updated NOx emission and TROPOMI NO$_2$ provides a basis for

337   further analyzing the mechanism of aggravated surface O$_3$ pollution.

338
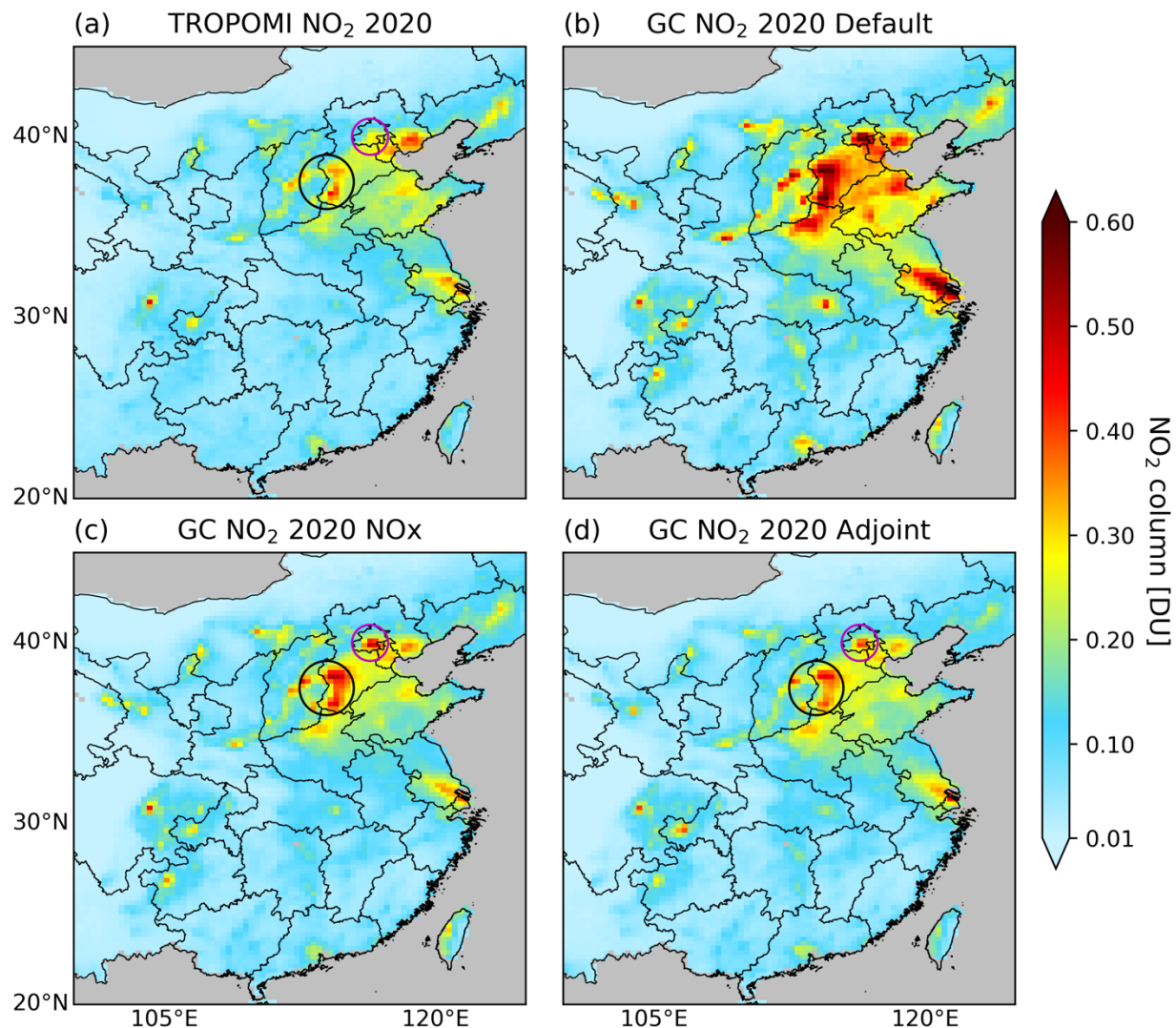
339 **Figure 3.** Comparison of tropospheric NO₂ VCD from (a) TROPOMI product in 2020 Feb.-Mar

340 with that from GEOS-Chem simulations (b) 2020 Default, (c) 2020 NOx and (d) 2020 Adjoint.

341 The pink and black circles mark the areas where NOx emissions from 4D-Var mitigated the NO₂

342 overestimation by mass balance method. The emissions and meteorology configurations for

343 GEOS-Chem simulations 2020 Default, 2020 NOx and 2020 Adjoint are listed in Table 1.

344
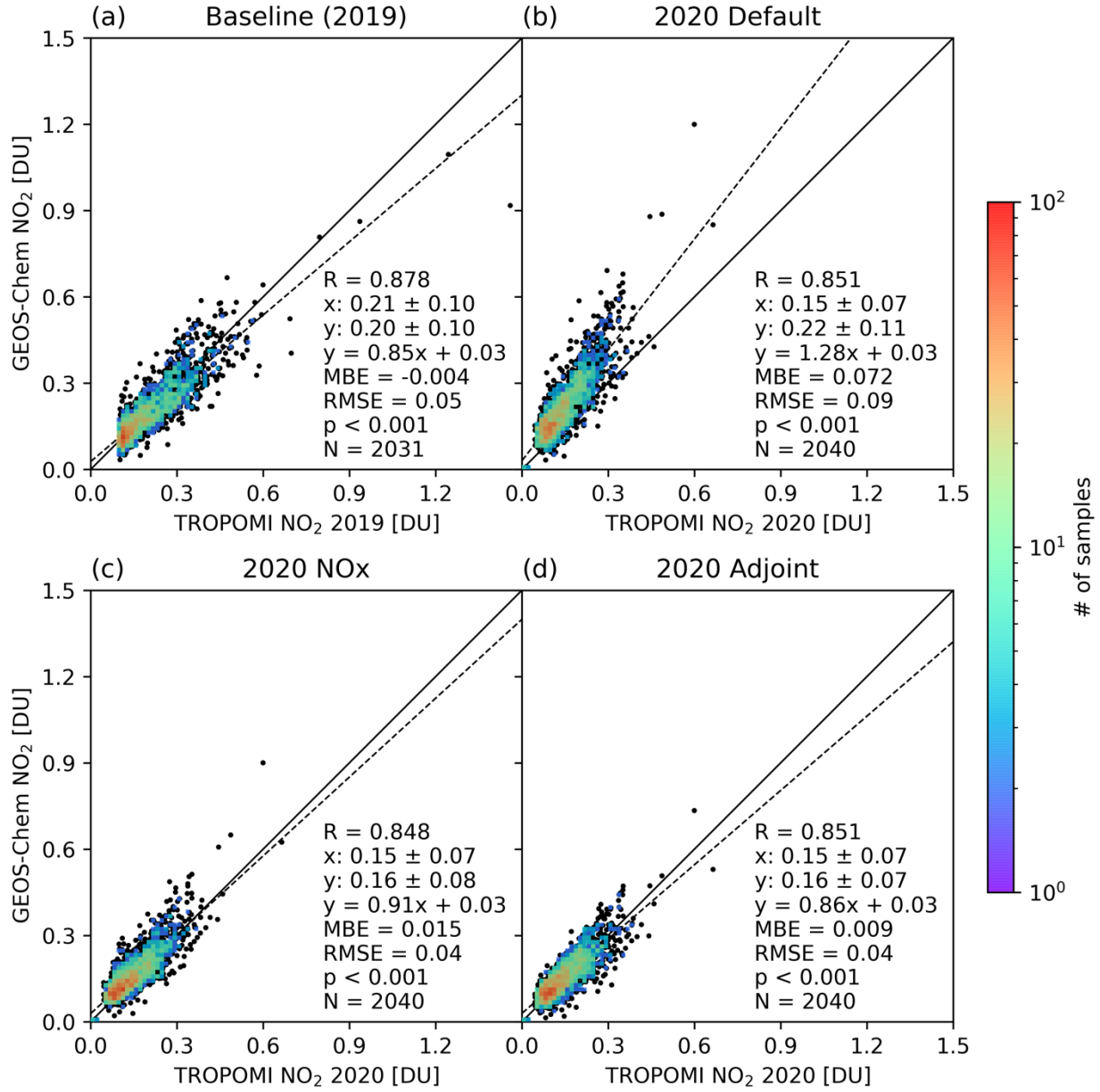
Figure 4. Scatter plot of TROPOMI NO$_2$ VCD versus the GEOS-Chem simulations for (a) Baseline (2019), (b) 2020 Default, (c) 2020 NOx and (d) 2020 Adjoint, respectively. TROPOMI data in Feb.-Mar. of 2019 was used in (a), and that of 2020 was used in (b-d). The emissions and meteorology configurations for GEOS-Chem simulations are listed in Table 1. Only pixels with TROPOMI NO$_2$ VCD in 2019 Feb.-Mar. larger than 0.1 DU are included in all comparisons.

353   Fig. 5 and Fig. 6 show the comparison of surface NO_2 between ground measurements and

354   GEOS-Chem simulations. The GEOS-Chem simulations Baseline (2019) (Fig. 5(b)) and 2020

355   Adjoint (Fig. 5(d)) both capture the spatial pattern and magnitude of surface NO_2 measurements

356   in Feb.-Mar. of 2019 (Fig. 5(a)) and 2020 (Fig. 5(c)) well, respectively. Fig. 6 further displays the

357   good agreements of surface NO_2 from Baseline (2019) (Fig. 6(a)) and 2020 Adjoint (Fig. 6(b)) to

358   the in-situ measurements via scatter plots. Table 2 displays the evaluation statistics, including the

359   correlation coefficient (R), MBE, RMSE and the slope and intercept of the linear regression, for

360   the simulated surface NO_2 from various simulation experiments compared with the in-situ

361   measurements. The correlation coefficient, MBE and RMSE between the simulation Baseline

362   (2019) and ground measurements in 2019 Feb.-Mar. are 0.724, 1.572 $\mu g\ m^{-3}$ and 8.49 $\mu g\ m^{-3}$,

363   respectively. Without updating the NOx emissions in 2020, the simulation 2020 Default

364   overestimate the ground measurements of surface NO_2 in 2020 Feb.-Mar (Table 2). The slope for

365   the linear regression is 1.19, and the MBE and RMSE are 6.021 $\mu g\ m^{-3}$ and 10.43 $\mu g\ m^{-3}$,

366   respectively (Table 2). After updating the NOx emissions, the GEOS-Chem simulations 2020 NOx

367   and 2020 Adjoint have good agreements with the in-situ measurements in 2020 Feb.-Mar. The

368   correlation coefficient between the simulation 2020 Adjoint versus the in-situ measurements is

369   0.651, higher than that of 0.608 for the simulation 2020 NOx versus the ground measurements

370   (Table 2). The MBE and RMSE of 2020 Adjoint (0.683 $\mu g\ m^{-3}$ and 6.68 $\mu g\ m^{-3}$) are lower than

371   those of 2020 NOx (1.726 $\mu g\ m^{-3}$ and 7.74 $\mu g\ m^{-3}$) (Table 2). This result further indicates the

372   superiority of 4D-Var for optimizing NOx emissions compared with the mass balance method

373   (Cooper et al., 2017; Streets et al., 2013).

374
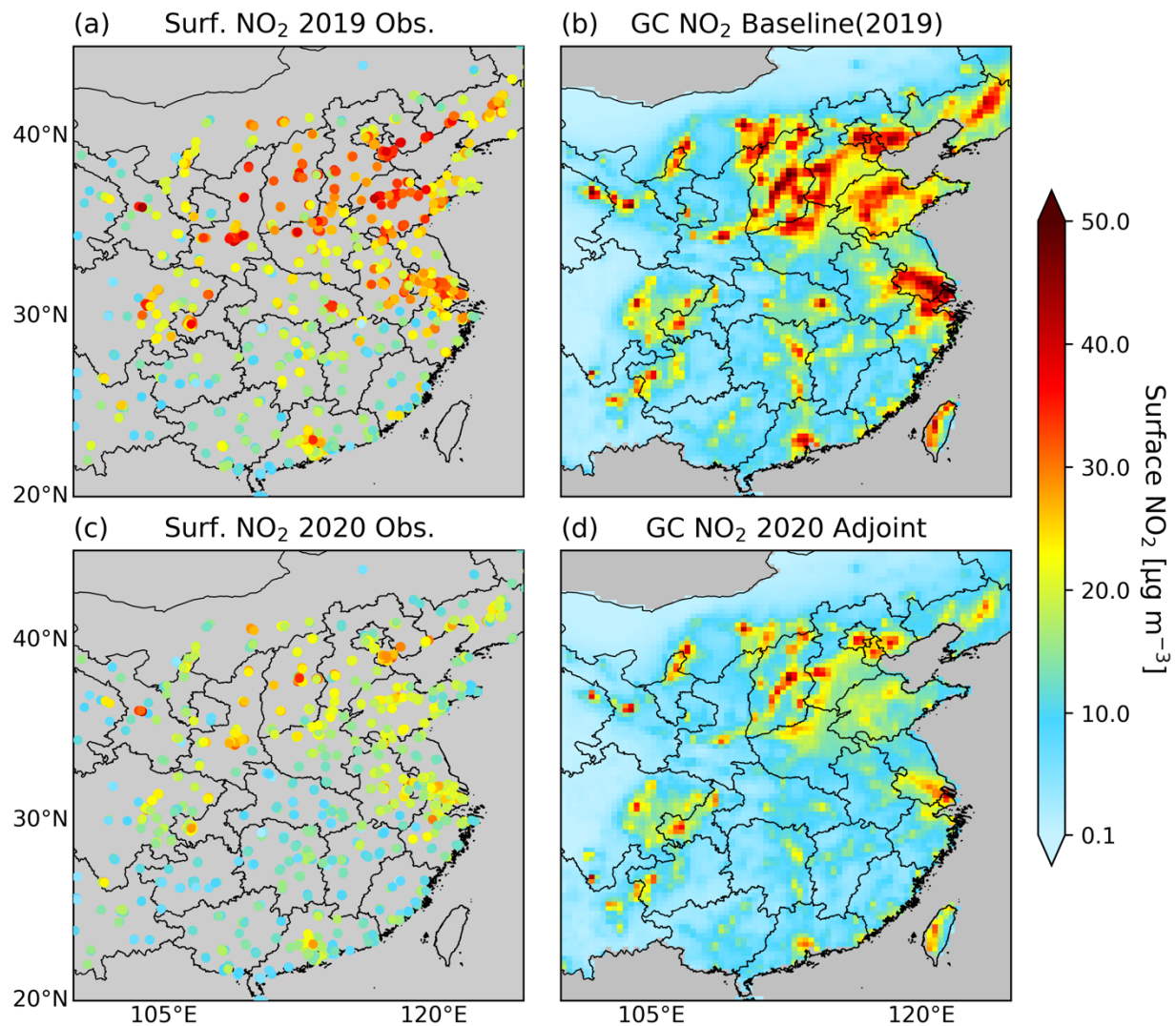
Figure 5. Comparison of surface NO$_2$ concentrations from ground measurements for (a) 2019 Feb.-Mar. and (c) 2020 Feb.-Mar. versus those from GEOS-Chem simulations (b) Baseline (2019) and (d) 2020 Adjoint. Grey color means no data is presented.

380
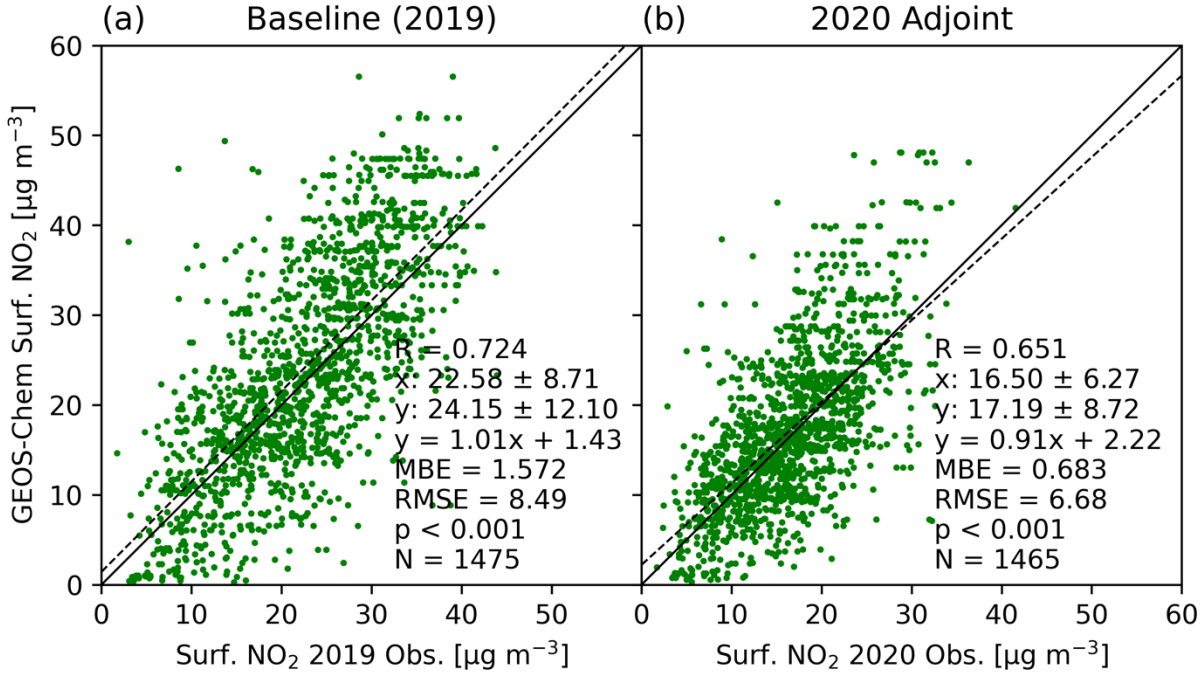
381 **Figure 6.** Scatter plots for comparing the surface NO₂ concentrations from GEOS-Chem

382 simulations and ground measurements. (a) GEOS-Chem simulation Baseline (2019) versus ground

383 measurements in 2019 Feb.-Mar. (b) GEOS-Chem simulation 2020 Adjoint versus ground

384 measurements in 2020 Feb.-Mar. Note: the number of ground sites differ in these two years.

385

386

387 **Table 2.** Evaluation statistics for modeled surface NO₂ compared with the in-situ measurements*.

Experiments	R	MBE ($\mu g\ m^{-3}$)	RMSE ($\mu g\ m^{-3}$)	Slope	Intercept ($\mu g\ m^{-3}$)
Baseline (2019)	0.724	1.572	8.49	1.01	1.43
2020 Default	0.661	6.021	10.43	1.19	2.95
2020 NOx	0.608	1.726	7.74	0.92	3.03
2020 Adjoint	0.651	0.683	6.68	0.91	2.22

388 * The simulation experiment Baseline (2019) is compared with the ground measurements in 2019

389 Feb.-Mar. Other three experiments are compared with the ground measurements in 2020 Feb.-Mar.

390

391 Fig. 7 (a) is the Taylor diagram for evaluating the GEOS-Chem simulations of surface NO₂

392 concentrations from 2020 Default, 2020 NOx and 2020 Adjoint using the in-situ measurements.

393   The simulation 2020 Adjoint (inverted triangle in Fig. 7(a)) has the best performance among these
394   three simulations with the lowest relative bias and lowest normalized centered RMSE. Without
395   updating the NOx emission, 2020 Default features a relative bias of ~37%. After updating the NOx
396   emissions, 2020 NOx reduces the relative bias, normalized centered RMSE and normalized
397   standard deviation from around 37%, 1.38 and 1.80 to around 10%, 1.20 and 1.51 compared with
398   2020 Default, but the correlation coefficient also decreases. By using 4D-Var method, 2020
399   Adjoint further reduces the relative bias, normalized centered RMSE and normalized standard
400   deviation and increases the correlation coefficient compared with 2020 NOx. We also validated
401   the VOC emissions by comparing the simulated HCHO VCD with TROPOMI measurements
402   (Appendix D).

403

404
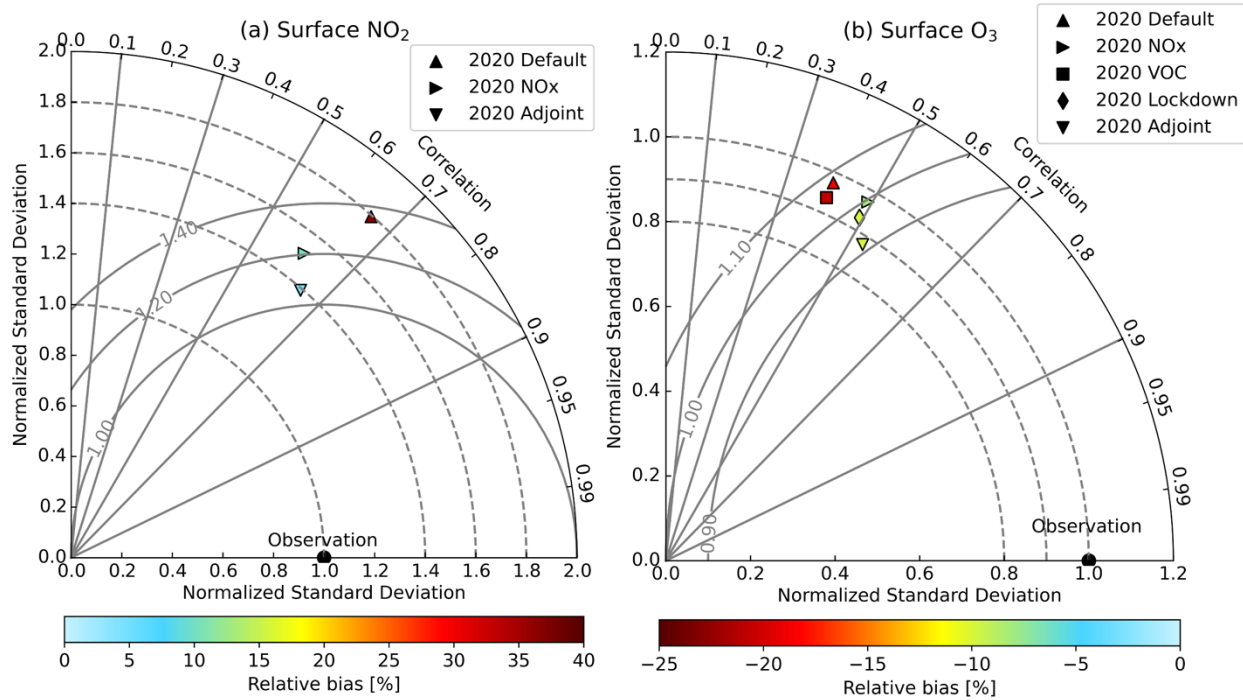
405 **Figure 7.** Taylor diagram for evaluating the GEOS-Chem simulations of (a) surface NO_2 and (b)
406 surface O_3 during lockdown period (2020 Feb.-Mar.) using ground observations for different
407 simulation experiments listed in Table 1. The evaluation of surface O_3 only includes the areas
408 where the NOx emissions optimized by 4D-Var reduced by more than 10%.

409

410

411 **3.3 Evaluation of surface O_3 simulations**

412   We evaluated the GEOS-Chem simulations of MDA8 surface O_3 from different simulation

413   experiments listed in Table 1 using ground measurements. Fig. 7(b) is the Taylor diagram for

414   comparing the surface O_3 concentrations during 2020 Feb.-Mar. from ground measurements and

415   GEOS-Chem simulations. We focused on areas with significant NOx emissions reduction to better

416   assess the role of updated NOx emissions in improving surface O_3 simulations. The ground sites

417   where the NOx emissions from 4D-Var decline by less than 10% are excluded. The correlation

418   coefficient between the simulation Baseline (2019) and ground observations is ~0.53 and the

419   relative bias is around -25%. By applying 2020 meteorological fields and scaling the VOC

420   emissions, the correlation coefficients decreased to ~0.40 for model simulations 2020 Default and

421   2020 VOC, with little reduction in the relative bias. By updating the NOx emissions, the relative

422   bias reduced to around -10% while the correlation coefficients remain at ~0.50 for model

423   simulations 2020 NOx, 2020 Lockdown and 2020 Adjoint. This indicates the NOx emission

424   updates significantly improve the surface O_3 simulations. Comparing the simulations 2020 Default

425   and 2020 VOC, or 2020 NOx and 2020 Lockdown, the results show that scaling VOC emissions

426   does not improve the surface O_3 simulations significantly over the continental China, but over

427   South China, VOC emissions update reduces the relative bias by 3%. Among all simulations, 2020

428   Adjoint exhibits the best performance with the lowest normalized centered RMSE, largest

429   correlation coefficient and a low relative bias of ~10%. This result further confirms the superiority

430   of the 4D-Var with respect to the mass balance method for optimizing NOx emissions. Therefore,

431   we used the 2020 Adjoint to evaluate the impacts of NOx emission on surface O_3 in the following

432   analysis.

433   Fig. 8 compares the modeled surface O_3 in Feb.-Mar. of 2019 (Fig. 8(a)) and 2020 (Fig.

434   8(b)) and the relative difference (Fig. 8(c)) computed from Equation (6) with the in-situ

435   measurements (Fig. 8(d-f)). The ground observations show that the highest level of surface O_3

436   pollution occurs in North China and southwest of China. The average MDA8 O_3 in two months

437   can reach up to ~110 $\mu g\ m^{-3}$ at STP (~51.4 ppbv), which is higher than the China National Ambient

438   Air Quality Standard daily maximum 8-hour Grade I standard of 100 $\mu g\ m^{-3}$. GEOS-Chem model

439   underestimates the surface O_3 over North China for both years compared with ground observations,

440   which could be a result of the underestimation of biogenic VOC emissions (Appendix D). The

441   underestimation of the simulated O_3 over North China will not significantly affect our study

442   purpose since this study focuses on revealing the impacts of emissions and meteorology change

443 on the surface O_3 change by each region. The bias is predominantly systematic and will be
444 substantially cancelled when we compute the relative difference of the surface O_3. The model
445 captures the magnitude and spatial distribution of surface O_3 and the increasing trend in South
446 China well. In South China, the measured surface O_3 in 2020 Feb.-Mar. increases by 30-50%,
447 while over North China, it increases generally by less than 20% even decreases in some regions.
448 The relative differences of simulated surface O_3 between two years is comparable to the ground
449 observations over South China (green box in Fig. 8(c, f)). In Sichuan Basin, the trend of the surface
450 O_3 change from the model is opposite to the measurements, which is probably caused by the
451 inaccurate simulation of the meteorological effects (See Section 4.1) due to the complex terrain
452 features in this region. The localized improvement of the model simulation is further needed for
453 the regional study. Over North China (pink box in Fig. 8(c, f)), the average relative difference
454 between two years from the model and observation are 4.27% and -3.01%, respectively, both of
455 which are much smaller than their counterparts in South China. While the relative difference from
456 model simulations has different signs as compared to that of observations on average, both the
457 change of O_3 is indeed small and the model is able to capture the part of O_3 decrease in the
458 southwest part of the North China domain (Fig. 8(c)). We note that some previous studies showed
459 large increase of O_3 in North China, but such increase is in comparison with the O_3 in the month
460 right before the lockdown (not the same time in 2019; (Shi & Brasseur, 2020; Y. M. Liu et al.,
461 2021).
462

463
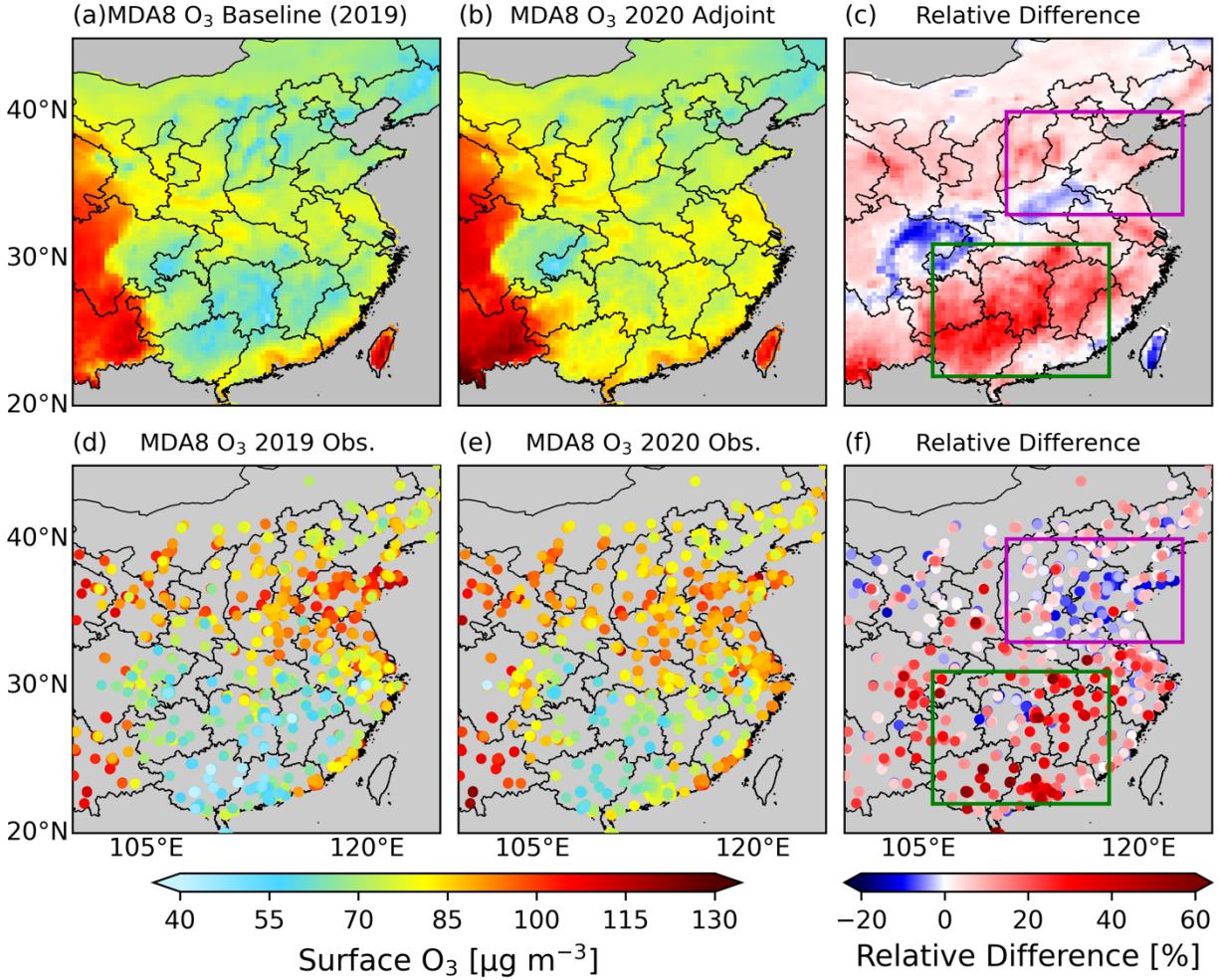
Figure 8. Comparison of MDA8 surface O_3 in 2019 and 2020 Feb.-Mar. and the relative difference

between two years from GEOS-Chem model (a-c) versus ground observations (d-f). GEOS-Chem

mean MDA8 O_3 at 9 m above the surface under standard temperature and pressure (STP; 273.15

K, 101.325 kPa) from (a) Baseline (2019) and (b) 2020 Adjoint simulation (Table 1) together with

(c) their relative difference. Ground observed mean MDA8 surface O3 under STP in (d) 2019 Feb.-

Mar.; (e) 2020 Feb.-Mar. and (f) their relative difference. The pink and green boxes in (c) and (f)

define the North China and South China domain.

4. Mechanism of aggravated surface O_3 pollution

4.1 Relative contribution from declining emissions and meteorological variations

475   From equations (2)-(5) we can analyze the mechanism of surface O$_3$ increase in China
476   during the COVID-19 pandemic (Fig. 9). NOx emission reduction as a result of COVID-19
477   lockdown leads to a ~8% increase in the mean MDA8 surface O$_3$ over North China (pink boxes in
478   Fig. 9) between 2019 and 2020 Feb.-Mar. (Fig. 9(a)), while the VOC emission decline causes ~3%
479   of O$_3$ decrease (Fig. 9(b)). The average contribution of the meteorological variations to the surface
480   O$_3$ change is less than 1% in North China (Fig. 9(d)). However, in South China, the inter-annual
481   meteorological variations dominate the surface O$_3$ increases, causing a ~30% increase (Fig. 9(d)),
482   while the NOx and VOC emission reduction has little impacts. The overall magnitude of emissions
483   contribution to the surface O$_3$ change over North China is ~5%, similar to that of the
484   meteorological effects, but meteorological variations lead to both O$_3$ increases and decreases in
485   different regions. Over South China, the meteorological effect is much larger than the net effects
486   of declining emissions. Overall, the impact of inter-annual meteorological variations between 2019
487   and 2020 is almost 30 times larger than the overall emissions impacts on the aggregated surface
488   O$_3$ pollution in China.

489   Our results are consistent with the conclusion from Zhao et al. (2020) that meteorological
490   variation has larger impacts than emissions reduction on surface O$_3$ in the southern city of
491   Guangzhou, but in Beijing, emission reduction has a larger impact during 23-29 January. Wang et
492   al. (2022) also showed ~80% of the O$_3$ MDA8 increase during the COVID lockdown period is
493   caused by the meteorological factors, and ~20% is caused by the emission decline in East China.
494   Liu et al. (2020b) reported that the surface O$_3$ increase in the major cites of the Yangtze River
495   Delta region were driven by both emission reduction and meteorological variations to a similar
496   degree from pre-lockdown period (Jan. 1-22, 2020) to lockdown period (Jan. 23-Feb. 29, 2020).
497   However, Zhao et al. (2020), Wang et al. (2022) and Liu et al. (2020b) only focused on the
498   lockdown period of one to five weeks in reference to the time period right before the lockdown
499   instead of the same period in previous years, which cannot exclude the effects of seasonal variation
500   of meteorology and did not provide a comprehensive analysis over the whole lockdown period,
501   and Zhao et al. (2020) and Liu et al. (2020b) did not separate the effects of seasonal trend from the
502   meteorological anomalies. Moreover, Liu et al. (2020b) and Wang et al. (2022) only analyzed four
503   representative cities or the East China region instead of showing the analysis at a national scale.
504   Further, Zhao et al. (2020) did not update the anthropogenic emissions during the lockdown period,
505   which brings significant uncertainties to their analysis. Previous studies found that TROPOMI

NO2 product has a negative bias of -7% to -20% (Verhoelst et al., 2021; Judd et al., 2020; Li et al., 2021). The sensitivity simulations indicate this low bias does not significantly affect the model evaluation and our main conclusions (figures not shown).
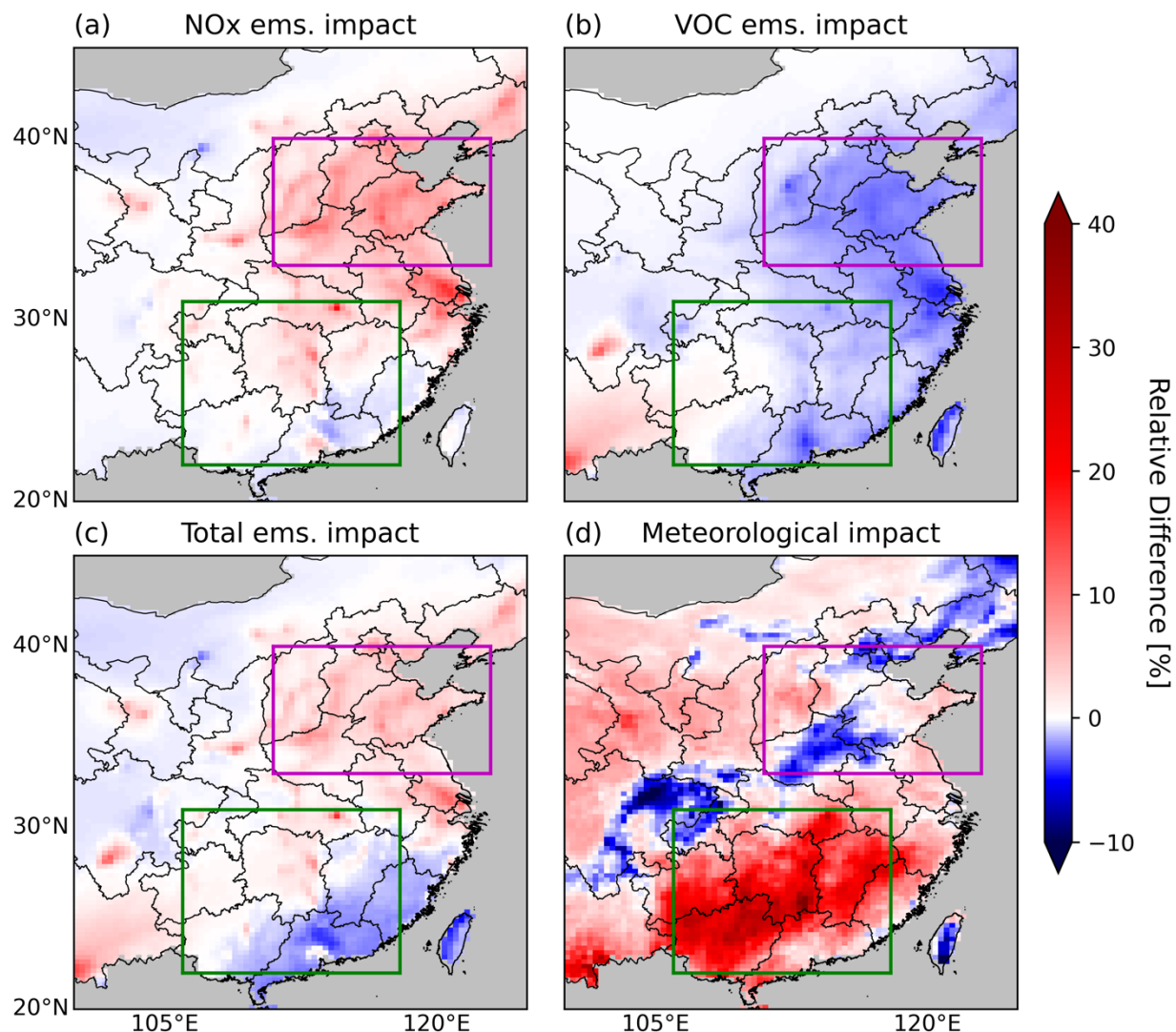
Figure 9. Relative difference in simulated surface O_3 caused by (a) NOx emission reduction, (b) VOC emission reduction, (c) overall emission reduction and (d) meteorological variations due to COVID-19 lockdown. The pink and green boxes in each panel define the North China and South China domain.

4.2 Critical meteorological variables causing aggravated surface O₃ pollution in South China

To identify the critical meteorological variables that lead to the aggravated surface O_3 pollution in South China, we investigated the correlations between the surface O_3 concentrations and 2-m air temperature, downward visible direct flux at surface, cloud fraction, relative humidity, and wind speed. The positive correlation between the surface O_3 and temperature is widely observed and reported in the literature (Pusede et al., 2015). Higher temperature leads to higher concentrations of surface O_3 because it improves the O_3 production rate by affecting the organic reactivity, production of HOx radicals, formation and decomposition of peroxy nitrates and alkyl nitrates (Pusede et al., 2015). We calculated the daily difference in Feb.-Mar. between 2020 and 2019 (excluding Feb. 29, 2020) for the daily mean of MDA8 O_3 from ground measurements and 2-meter air temperature, downward visible direct flux at surface and cloud fraction from GEOS-FP data used in our GEOS-Chem simulations for the South China (106°E - 118°E, 22°N - 31°N, green box in Fig. 10(a-c)) and North China (111°E - 123°E, 33°N - 40°N, pink box in Fig. 10(a-c)). Fig. 10 displays the difference of 2-month mean 2-meter air temperature (Fig. 10(a)), downward visible direct flux at surface (Fig. 10(b)) and cloud fraction (Fig. 10(c)) in Feb.-Mar. between 2020 and 2019 and the scatter plot between the daily difference of measured surface O_3 concentration and 2-meter air temperature (Fig. 10(d)), downward visible direct flux at surface (Fig. 10(e)) and cloud fraction (Fig. 10(f)) over both South China (green dots in Fig. 10(d-f)) and North China (pink dots in Fig. 10(d-f)). We found the 2-meter air temperature increased by ~2.3°C in South China, and the daily difference of surface O_3 concentration and 2-meter air temperature are well correlated with a positive correlation coefficient of 0.612. Therefore, the temperature increase contributed to the significant aggravated surface O_3 pollution in South China. The enhanced solar radiation at surface could also promote the production of O_3 via photochemical reactions. The correlation coefficient between the daily difference of surface O_3 concentration and downward visible direct flux at surface is as high as 0.740 in South China (Fig. 10(e)). The reason for the increase of temperature and solar radiation at surface is the lower cloud fraction. Via analyzing the GEOS-FP data, we found the cloud fraction decreases by ~5% (Fig. 10(c)), and the downward visible direct flux at surface increased by 5 W m⁻² (Fig. 10(b)) over South China. The lower cloud fraction increases the downward solar radiation at the surface during the lockdown period, leading to higher surface air temperature. The change of cloud fraction is negatively

548   correlated with the change of surface O_3 in South China with the correlation coefficient of -0.619

549   (Fig. 10(f)).

550   In North China, 2-meter air temperature also increased by 1.8°C, but the measured surface

551   MDA8 O_3 decreased by 3% (Fig. 8(f)). Fig. 10(d) shows the daily difference of MDA8 O_3 and 2-

552   meter air temperature over North China also has a high correlation coefficient of 0.731. However,

553   the intercept of the linear regression line is negative, so that the surface O_3 could decrease even

554   though the temperature increases. This negative intercept is caused by the net effects of factors

555   other than temperature, including chemistry, emissions, and other meteorological factors. It is a

556   challenge to quantify the contributions of each individual factors, because these factors are

557   thermodynamically or dynamically related. The predicted average change of surface MDA8 O_3 in

558   South China and North China are marked by the green and pink open squares respectively in Fig.

559   10(d) based on the linear regression. Because of the different intercepts, the predicted MDA8 O_3

560   in South China increases by ~9.0 µg m^{-3}, while it decreases by 2.2 µg m^{-3} in North China, although

561   the average temperature increased in both South and North China. On the contrary to South China,

562   the change of solar radiation at surface and cloud fraction are poorly correlated with the change of

563   surface O_3 concentrations in North China (Fig. 10(e, f)), mainly due to a more important role of

564   emission change in regulating the surface O_3 in North China.

565
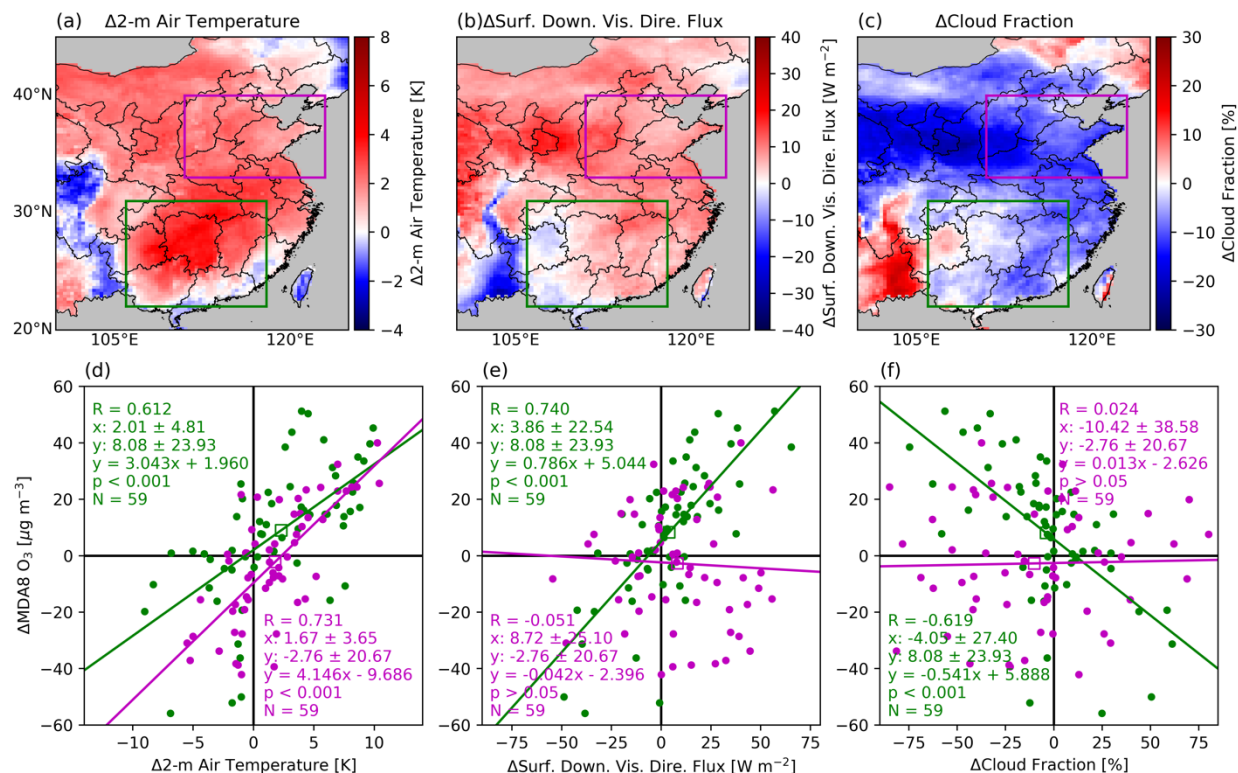
Figure 10. The changes of (a) 2-meter air temperature, (b) downward visible direct flux at surface and (c) cloud fraction from 2019 Feb.-Mar. to 2020 Feb.-Mar and the scatter plots between the daily difference of surface O_3 measurements and (d) 2-meter air temperature, (e) downward visible direct flux at surface and (f) cloud fraction in Feb.-Mar. between 2020 and 2019 over South China (green dots) and North China (pink dots). The green and pink open squares in (d-f) mark the predicted average change of surface MDA8 O_3 in South China and North China, respectively, based on the linear regression against the change of meteorological variables.

The impacts of relative humidity and wind speed on the surface O_3 change are also investigated (Fig. 11). The relative humidity increased by ~5.1% in North China and decreased by ~3.0% in South China on average. The strong correlation (R = -0.675) between the change of relative humidity and surface O_3 in South China indicates the decrease of relative humidity also contributes to the increase of surface O_3 pollution in South China, but the correlation between them in North China is very low. The wind speed also changed oppositely in South China and North China, but we cannot identify any significant impact of wind speed on the surface O_3 pollution since the correlation coefficients are low in both South China and North China. In summary, the significant increase of surface O_3 pollution during the lockdown period in South China could be

584   primarily attributed to the higher temperature, enhanced solar radiation at surface and declined

585   relative humidity.

586
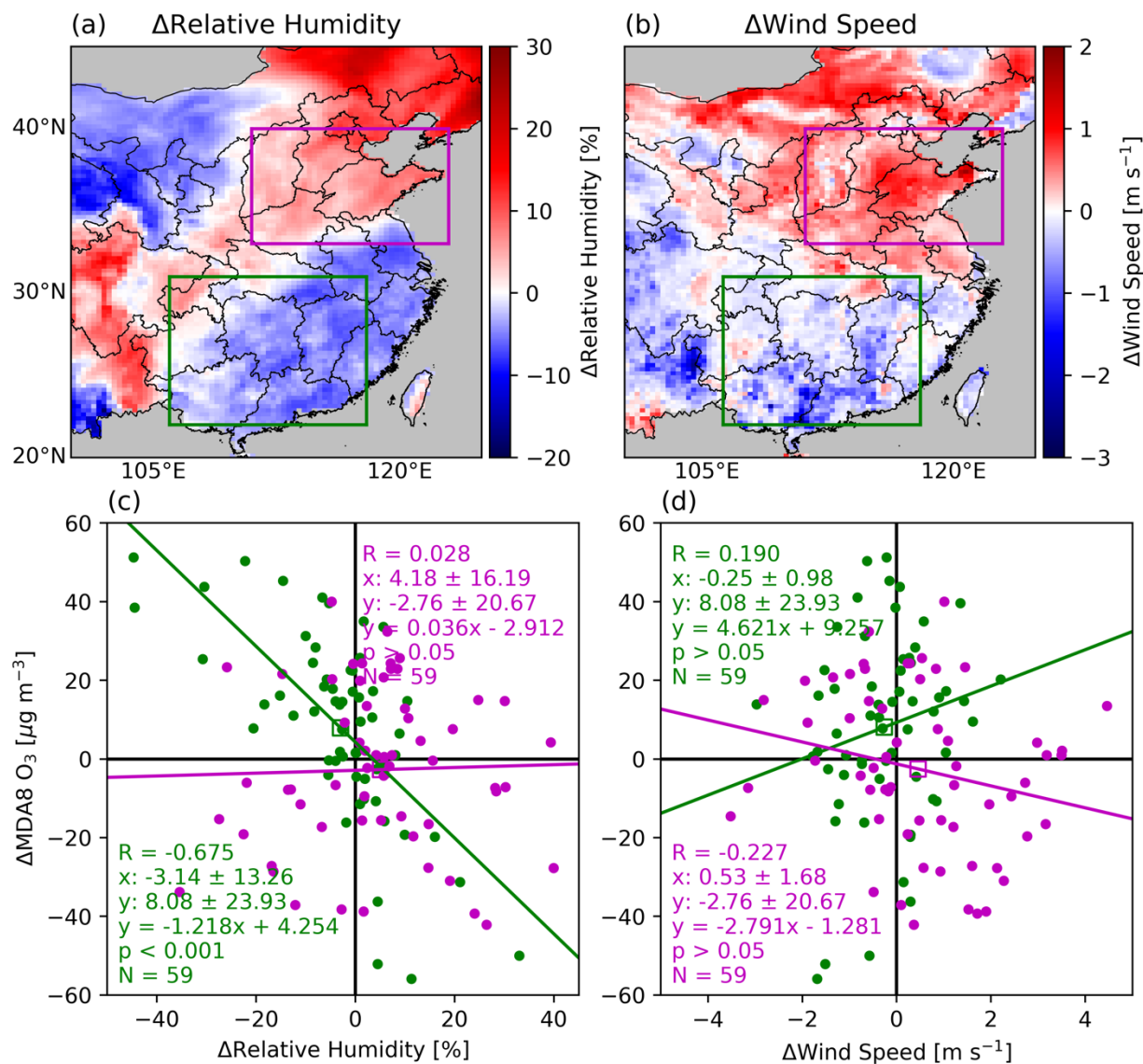
587   **Figure 11.** Same as Fig. 10 but for (a, c) relative humidity and (b, d) wind speed.

588

5. Summary

590   A significant reduction in primary air pollutants has been identified by surface and satellite

591   observations during the COVID-19 pandemic in China (Bauwens et al., 2020; Miyazaki et al.,

592   2020), which is in contrast to the increase of surface O_3. In this study, we analyzed the reasons for

593   the enhanced surface O_3 pollution from two perspectives: anthropogenic emissions reduction and

594   inter-annual meteorological variations. We constrain the NOx emissions based on the TROPOMI

595   NO$_2$ product using both the mass balance and 4D-Var methods. The VOC emissions were also

596   updated based on the TROPOMI HCHO product via the mass balance approach. We analyzed the

597   contributions from emissions reduction and meteorological variations to surface O$_3$ increases

598   through a series of sensitivity simulations using the GEOS-Chem model.

599   The updated NOx emissions from the 4D-Var and mass balance approaches share a similar

600   spatial pattern. However, the NOx emissions from 4D-Var are lower than those from the mass

601   balance method over North China by ~10% but larger over central China by ~40%. The evaluation

602   of the simulations with the updated emissions against the TROPOMI NO$_2$, in-situ measurements

603   of surface NO$_2$ and O$_3$ indicate that the NOx emissions from the 4D-Var inversion leads to better

604   model performance than that from the mass balance approach. The updated anthropogenic VOC

605   emissions with mass balance method are evaluated by comparing the GEOS-Chem HCHO and

606   TROPOMI HCHO. However, the updated VOC emissions may still suffer from large uncertainties

607   because of the low retrieval accuracy of TROPOMI HCHO (Vigouroux et al., 2020), large

608   biogenic sources of VOC emissions and limited representativeness of HCHO for the whole VOC

609   species.

610   The anthropogenic NOx emission decreased by ~30% over East China during 2020 Feb.-

611   Mar. compared to the same period in 2019. Over North China, NOx emission reduction leads to a

612   ~8% increase in the mean MDA8 surface O$_3$, while the VOC emissions decline causes O$_3$ to

613   decrease by ~3%. The average contribution of meteorological variations to the surface O$_3$ change

614   is less than 1% in North China. However, in South China, the inter-annual meteorological variation

615   dominates the surface O$_3$ increase, causing a ~30% increase, while the NOx and VOC emission

616   reduction has nearly no impacts on O$_3$. Overall, the impact of inter-annual meteorological

617   variations between 2019 and 2020 is almost 30 times larger than the impact of emissions on the

618   enhanced surface O$_3$ pollution in China.

619   The significant increase of surface O$_3$ in South China could be attributed to the higher

620   temperature, enhanced solar radiation at surface and declined relative humidity during the

621   lockdown period. The lower cloud fraction increases the downward solar radiation at the surface

622   during the lockdown period, leading to higher surface air temperature. We cannot identify any

623   significant impact of wind speed on the surface O$_3$ pollution.

624

625

Appendix A: NOx emission reduction in China from 2010 to 2019

The default anthropogenic NOx emission over East Asia in GEOS-Chem is MIX 2010 (Li et al., 2017).To generate the anthropogenic NOx emission in 2019, we calculated the ratio of mean TROPOMI tropospheric NO_2 VCD in Feb.-Mar. 2019 to GEOS-Chem simulated NO_2 VCD with the default MIX 2010 emission as the scaling factor (Fig. A1). The scaling factors in regions where mean TROPOMI tropospheric NO_2 VCD in 2019 Feb.-Mar. less than 0.1 DU are set to 1. From 2010 to 2019, the anthropogenic NOx emission has declined significantly as a result of the clean air actions of Chinese government (Zheng et al., 2018).
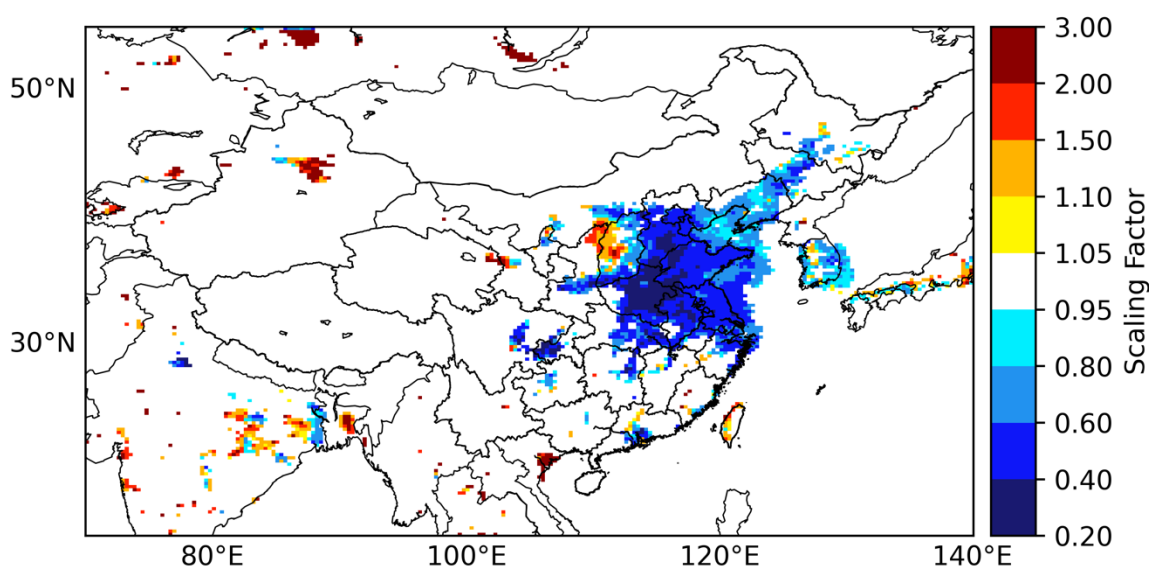
Figure A1. The scaling factor of anthropogenic NOx emission from year 2010 to 2019.

Appendix B: Applying the TROPOMI NO₂ averaging kernel in the observation operator

To optimize the NOx emissions and minimize the cost function (Equation (1)) with the 4D-Var method, GEOS-Chem adjoint needs to compute the derivative of the cost function with respect to the model parameters to be optimized, which is the scaling factors of the anthropogenic NOx emissions in this study. An essential step is to calculate the adjoint forcing $\boldsymbol{F}$, which is the derivative of the cost function with respect to the modeled NO_2 concentration shown as Equation (B1).

647
$$\boldsymbol{F} = \frac{\partial J}{\partial \boldsymbol{c}} = \boldsymbol{S}_{\text{obs}}^{-1}[H(\boldsymbol{c}) - \boldsymbol{s}]\frac{\partial H(\boldsymbol{c})}{\partial \boldsymbol{c}} \tag{B1}$$

648 For each single TROPOMI NO$_2$ observation, the adjoint forcing component f and cost function

649 component j are computed as Equation (B2) and Equation (B3).

650
$$f = \frac{M_{\text{gc}}v_{\text{gc}} - M_{\text{obs}}v_{\text{obs}}}{e_{\text{obs}}M_{\text{obs}}}M_{\text{gc}} \tag{B2}$$

651
$$j = \frac{0.5f\left(M_{\text{gc}}v_{\text{gc}} - M_{\text{obs}}v_{\text{obs}}\right)}{M_{\text{gc}}} \tag{B3}$$

652 Here M_{gc} is GEOS-Chem air mass factor applying the GEOS-Chem NO$_2$ vertical profiles and

653 TROPOMI NO$_2$ averaging kernel. M_{obs} is TROPOMI air mass factor. v_{gc} and v_{obs} are the

654 tropospheric NO$_2$ VCD from GEOS-Chem model and TROPOMI observation, respectively. The

655 product of air mass factor and NO$_2$ VCD is NO$_2$ slant column density. e_{obs} is the standard error of

656 TROPOMI tropospheric NO$_2$ VCD.

657   We calculated the GEOS-Chem air mass factor M_{gc} as Equation (B4) following Qu et al.

658 (2019).

659
$$M_{\text{gc}} = \frac{\sum_{i\in\text{trop.}} c_i^{\text{gc}}\Delta p_i^{\text{gc}}w_i^{\text{gc}}}{\sum_{i\in\text{trop.}} c_i^{\text{gc}}\Delta p_i^{\text{gc}}} \tag{B4}$$

660 Here c_i^{gc} is GEOS-Chem NO$_2$ mixing ratio at vertical layer i, Δp_i^{gc} is the pressure difference

661 between the GEOS-Chem vertical layer i and $i+1$. w_i^{gc} is the scattering weight at the GEOS-Chem

662 vertical layer i, which is calculated by the linear interpolation of the scattering weights at the

663 vertical coordinate of the model TM5 used for TROPOMI NO$_2$ retrieval. The scattering weight at

664 the TM5 vertical layer l (w_l^{TM5}) is computed as the product of TROPOMI air mass factor and the

665 TROPOMI averaging kernel at the TM5 vertical layer l (A_l^{TM5}) using Equation (B5-B6) (Eskes

666 and Boersma, 2003; Palmer et al., 2001).

667
$$w_l^{\text{TM5}} = \frac{M_{\text{obs}}A_l^{\text{TM5}}}{M_{\text{geo}}} \tag{B5}$$

668
$$M_{\text{geo}} = \sec\theta_0 + \sec\theta \tag{B6}$$

669 where M_{geo} is geometric air mass factor, θ_0 and θ are solar zenith angle and viewing zenith angle,

670 respectively.

671

672 **Appendix C: Validation of the TROPOMI NO$_2$ observation operator**

673   We validated the observation operator by comparing the sensitivity of the cost function

674   with respect to the emission scaling factor from GEOS-Chem adjoint and a finite difference

675   estimation as shown in Equation (C1). We shut down the transport and exclude a priori term from

676   the cost function for the validation, so that the gradient of cost function component in each grid

677   cell to the local emission scaling factor equals to the gradient of total cost function to the emission

678   scaling factor in the same grid cell.

679
$$\frac{\partial J(\ln \sigma)}{\partial \ln \sigma} \approx \frac{J(\ln(\sigma + 0.05)) - J(\ln(\sigma - 0.05))}{\ln(\sigma + 0.05) - \ln(\sigma - 0.05)} \qquad (C1)$$

680   Fig. C1 compared the cost function sensitivities calculated from GEOS-Chem adjoint and

681   the finite difference method for the nested grids with the spatial resolution of 0.25°×0.3125°. The

682   spatial pattern and magnitude of the cost function sensitivities from the two methods match with

683   each other with a correlation coefficient of 0.97. The statistics show that the agreement of the

684   adjoint sensitivities and finite difference sensitivities in this study is comparable to that in Wang

685   et al. (2020a) although we constrain the NOx emission at a much finer resolution of 0.25°×0.3125°

686   than in their study (2°×2.5°).

687
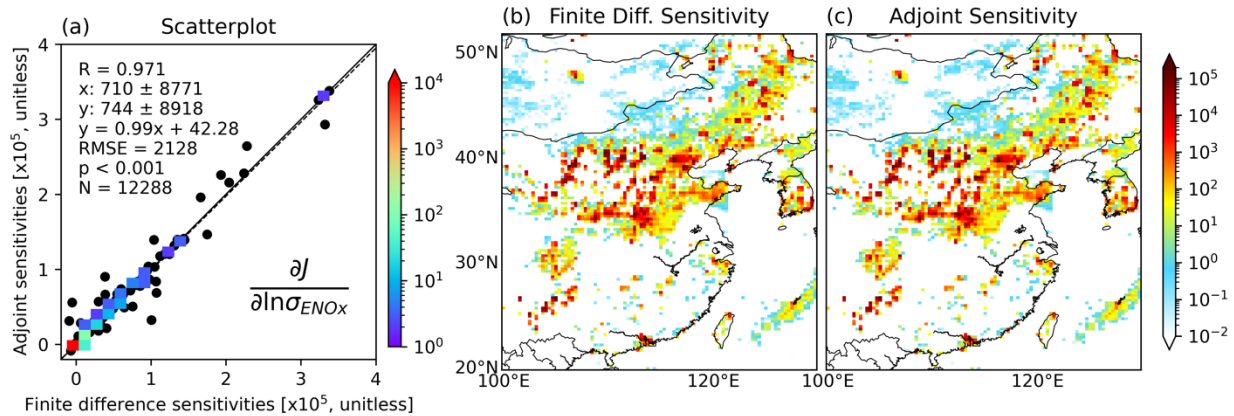
689   **Figure C1.** Comparison of adjoint sensitivities and finite difference sensitivities. (a) Scatter plot

690   of the adjoint sensitivity of the cost function with respect to the logarithm of NOx emission scaling

691   factor versus the finite difference sensitivities. The color scheme for panel (a) encodes the number

692   of samples (the legend on the right of panel (a)). (b) Map of finite difference sensitivity. (c) Map

693   of adjoint sensitivity.

694

695   **Appendix D: Validation of HCHO simulations**

696   It is not practical to validate the VOC emissions species by species in this study. We

697   compare the GEOS-Chem simulation of HCHO with TROPOMI data for a rough validation of the

698   VOC emissions. Overall, the GEOS-Chem simulations Baseline (2019) and 2020 Adjoint agree

699   well with TROPOMI HCHO in Feb.-Mar. of 2019 and 2020, respectively (Fig. D1). The

700   correlation coefficients for the two comparisons are 0.878 and 0.874, and the MBE are -0.036 DU

701   and -0.042 DU, respectively. This good agreement also supports our assumption of ignoring the

702   change of VOC emissions from 2010 to 2019, since the anthropogenic VOC emission used for

703   Baseline (2019) is equivalent to MIX 2010. However, Fig. D1 shows GEOS-Chem tends to

704   overestimate the HCHO VCD over urban regions and underestimate it over rural regions, which

705   indicates the partition of total emissions may overestimate the anthropogenic emissions and

706   underestimate the biogenic emissions, at least for HCHO. A more comprehensive evaluation for

707   various species and emission sectors would be helpful for further improvement of the VOC

708   emissions used in the model.

709

710
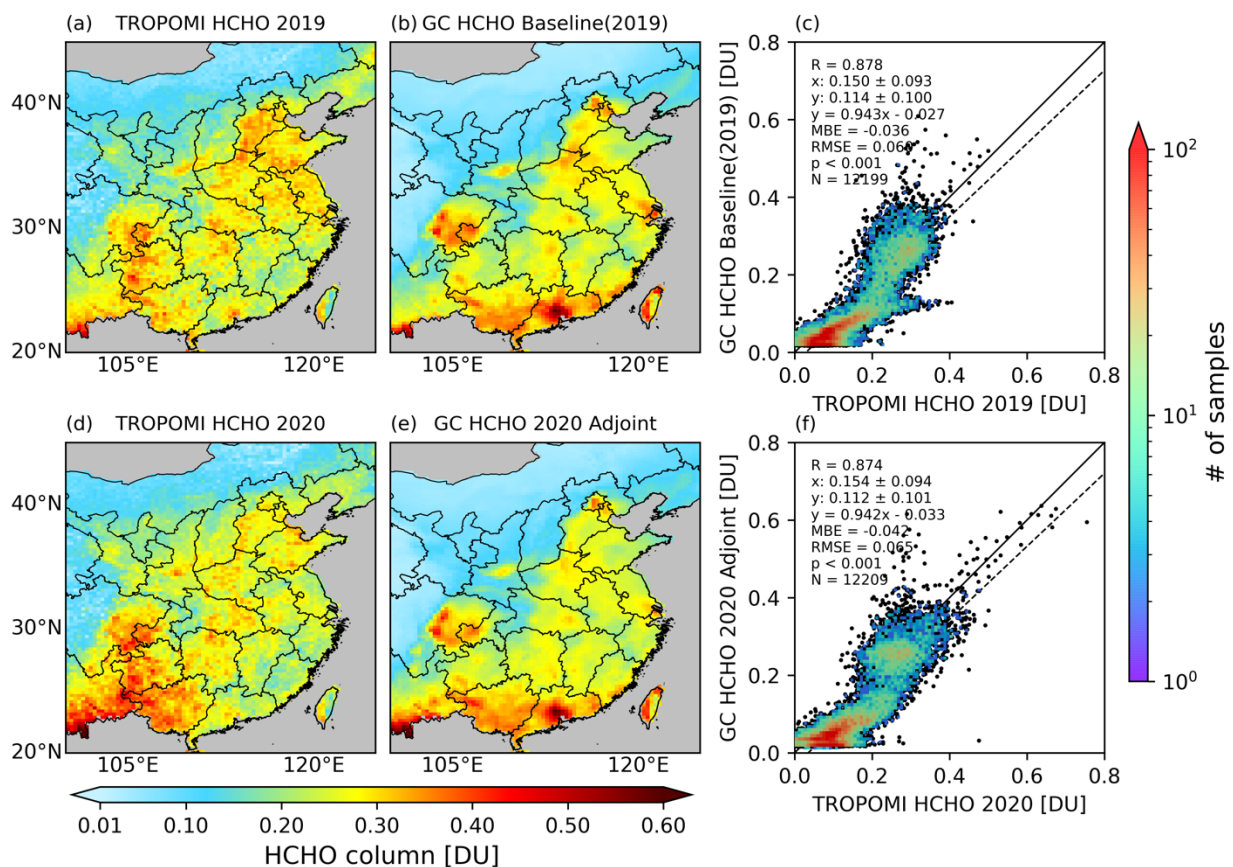
Figure D1. Comparison of tropospheric HCHO VCD from TROPOMI and GEOS-Chem. (a): TROPOMI HCHO in 2019 Feb.-Mar. (b): GEOS-Chem HCHO from Baseline (2019). (c): Scatter plot between (a) and (b). (d): TROPOMI HCHO in 2020 Feb. -Mar. (e): GEOS-Chem HCHO from 2020 Adjoint. (f): Scatter plot between (d) and (e). The emissions and meteorology configurations for GEOS-Chem simulations Baseline (2019) and 2020 Adjoint are listed in Table 1.

Data availability

The TROPOMI NO_2 and HCHO product are available at the NASA Goddard Earth Sciences Data and Information Services Center (https://daac.gsfc.nasa.gov). The ground O_3 and NO_2 measurements are available at the China National Environmental Monitoring Center (http://www.cnemc.cn/en/).

Author contribution

ZL and JW designed the research, and ZL conducted the research. YW, DKH and XC contributed to the research design. ZL and JW wrote the manuscript, and XC and DKH contributed to the writing. YW and TS developed the codes for comparing the tropospheric NO_2 VCD from model and TROPOMI data. KS developed the codes for oversampling.

Competing interests

The authors declare that they have no conflict of interest.

Acknowledgements

This research is supported by the NASA ACMAP program (grant number: 80NSSC19K0950). We acknowledge the computational support from the High-Performance Computing group at the University of Iowa.

References

Atkinson, R.: Atmospheric chemistry of VOCs and NOx, Atmospheric Environment, 34, 2063-2101, 10.1016/s1352-2310(99)00460-4, 2000.

Bauwens, M., Compernolle, S., Stavrakou, T., Muller, J. F., van Gent, J., Eskes, H., Levelt, P. F., van der A, R., Veefkind, J. P., Vlietinck, J., Yu, H., and Zehner, C.: Impact of Coronavirus Outbreak on NO2 Pollution Assessed Using TROPOMI and OMI Observations, Geophys Res Lett, 47, 10.1029/2020GL087978, 2020.

Bey, I., Jacob, D. J., Yantosca, R. M., Logan, J. A., Field, B. D., Fiore, A. M., Li, Q., Liu, H. Y., Mickley, L. J., and Schultz, M. G.: Global modeling of tropospheric chemistry with assimilated meteorology: Model description and evaluation, Journal of Geophysical Research: Atmospheres, 106, 23073-23095, 10.1029/2001jd000807, 2001.

Bi, Z., Ye, Z., He, C., and Li, Y.: Analysis of the meteorological factors affecting the short-term increase in O3 concentrations in nine global cities during COVID-19, Atmospheric Pollution Research, 13, 101523, https://doi.org/10.1016/j.apr.2022.101523, 2022.

Chen, D., Wang, Y., McElroy, M. B., He, K., Yantosca, R. M., and Le Sager, P.: Regional CO pollution and export in China simulated by the high-resolution nested-grid GEOS-Chem model, Atmospheric Chemistry and Physics, 9, 3825-3839, 10.5194/acp-9-3825-2009, 2009.

Cooper, M., Martin, R. V., Padmanabhan, A., and Henze, D. K.: Comparing mass balance and adjoint methods for inverse modeling of nitrogen dioxide columns for global nitrogen oxide emissions, Journal of Geophysical Research: Atmospheres, 122, 4718-4734, 10.1002/2016jd025985, 2017.

De Smedt, I., Theys, N., Yu, H., Danckaert, T., Lerot, C., Compernolle, S., Van Roozendael, M., Richter, A., Hilboll, A., Peters, E., Pedergnana, M., Loyola, D., Beirle, S., Wagner, T., Eskes, H., van Geffen, J., Boersma, K. F., and Veefkind, P.: Algorithm theoretical baseline for formaldehyde retrievals from S5P TROPOMI and from the QA4ECV project, Atmospheric Measurement Techniques, 11, 2395-2426, 10.5194/amt-11-2395-2018, 2018.

Eskes, H. J. and Boersma, K. F.: Averaging kernels for DOAS total-column satellite retrievals, Atmospheric Chemistry and Physics, 3, 1285-1291, 10.5194/acp-3-1285-2003, 2003.

Ghahremanloo, M., Lops, Y., Choi, Y., and Mousavinezhad, S.: Impact of the COVID-19 outbreak on air pollution levels in East Asia, Science of the Total Environment, 754, 10.1016/j.scitotenv.2020.142226, 2021.

772   Gong, C., Lei, Y., Ma, Y., Yue, X., and Liao, H.: Ozone–vegetation feedback through dry

773   deposition and isoprene emissions in a global chemistry–carbon–climate model, Atmos. Chem.

774   Phys., 20, 3841-3857, 10.5194/acp-20-3841-2020, 2020.

775   Guenther, A. B., Jiang, X., Heald, C. L., Sakulyanontvittaya, T., Duhl, T., Emmons, L. K., and

776   Wang, X.: The Model of Emissions of Gases and Aerosols from Nature version 2.1 (MEGAN2.1):

777   an extended and updated framework for modeling biogenic emissions, Geoscientific Model

778   Development, 5, 1471-1492, 10.5194/gmd-5-1471-2012, 2012.

779   Guo, J., Zhang, X. S., Gao, Y., Wang, Z. W., Zhang, M. G., Xue, W. B., Herrmann, H., Brasseur,

780   G. P., Wang, T., and Wang, Z.: Evolution of Ozone Pollution in China: What Track Will It Follow?,

781   Environmental Science & Technology, 57, 109-117, 10.1021/acs.est.2c08205, 2023.

782   Henze, D. K., Hakami, A., and Seinfeld, J. H.: Development of the adjoint of GEOS-Chem,

783   Atmospheric Chemistry and Physics, 7, 2413-2433, 10.5194/acp-7-2413-2007, 2007.

784   Henze, D. K., Seinfeld, J. H., and Shindell, D. T.: Inverse modeling and mapping US air quality

785   influences of inorganic PM2.5 precursor emissions using the adjoint of GEOS-Chem, Atmospheric

786   Chemistry and Physics, 9, 5877-5903, 10.5194/acp-9-5877-2009, 2009.

787   Hoesly, R. M., Smith, S. J., Feng, L., Klimont, Z., Janssens-Maenhout, G., Pitkanen, T., Seibert,

788   J. J., Vu, L., Andres, R. J., Bolt, R. M., Bond, T. C., Dawidowski, L., Kholod, N., Kurokawa, J.-

789   i., Li, M., Liu, L., Lu, Z., Moura, M. C. P., O'Rourke, P. R., and Zhang, Q.: Historical (1750–2014)

790   anthropogenic emissions of reactive gases and aerosols from the Community Emissions Data

791   System (CEDS), Geoscientific Model Development, 11, 369-408, 10.5194/gmd-11-369-2018,

792   2018.

793   Huang, X., Ding, A., Gao, J., Zheng, B., Zhou, D., Qi, X., Tang, R., Wang, J., Ren, C., Nie, W.,

794   Chi, X., Xu, Z., Chen, L., Li, Y., Che, F., Pang, N., Wang, H., Tong, D., Qin, W., Cheng, W., Liu,

795   W., Fu, Q., Liu, B., Chai, F., Davis, S. J., Zhang, Q., and He, K.: Enhanced secondary pollution

796   offset reduction of primary emissions during COVID-19 lockdown in China, National Science

797   Review, 8, 10.1093/nsr/nwaa137, 2020.

798   Hudman, R. C., Moore, N. E., Mebust, A. K., Martin, R. V., Russell, A. R., Valin, L. C., and

799   Cohen, R. C.: Steps towards a mechanistic model of global soil nitric oxide emissions:

800   implementation and space based-constraints, Atmospheric Chemistry and Physics, 12, 7779-7795,

801   10.5194/acp-12-7779-2012, 2012.

Janssens-Maenhout, G., Crippa, M., Guizzardi, D., Dentener, F., Muntean, M., Pouliot, G., Keating, T., Zhang, Q., Kurokawa, J., Wankmuller, R., van der Gon, H. D., Kuenen, J. J. P., Klimont, Z., Frost, G., Darras, S., Koffi, B., and Li, M.: HTAP_v2.2: a mosaic of regional and global emission grid maps for 2008 and 2010 to study hemispheric transport of air pollution, Atmospheric Chemistry and Physics, 15, 11411-11432, 10.5194/acp-15-11411-2015, 2015.

Jerrett, M., Burnett, R. T., Pope, C. A., Ito, K., Thurston, G., Krewski, D., Shi, Y. L., Calle, E., and Thun, M.: Long-Term Ozone Exposure and Mortality, New England Journal of Medicine, 360, 1085-1095, 10.1056/NEJMoa0803894, 2009.

Judd, L. M., Al-Saadi, J. A., Szykman, J. J., Valin, L. C., Janz, S. J., Kowalewski, M. G., Eskes, H. J., Veefkind, J. P., Cede, A., Mueller, M., Gebetsberger, M., Swap, R., Pierce, R. B., Nowlan, C. R., Abad, G. G., Nehrir, A., and Williams, D.: Evaluating Sentinel-5P TROPOMI tropospheric NO2 column densities with airborne and Pandora spectrometers near New York City and Long Island Sound, Atmospheric Measurement Techniques, 13, 6113-6140, 10.5194/amt-13-6113-2020, 2020.

Le, T. H., Wang, Y., Liu, L., Yang, J. N., Yung, Y. L., Li, G. H., and Seinfeld, J. H.: Unexpected air pollution with marked emission reductions during the COVID-19 outbreak in China, Science, 369, 702-706, 10.1126/science.abb7431, 2020.

Leue, C., Wenig, M., Wagner, T., Klimm, O., Platt, U., and Jähne, B.: Quantitative analysis of NOx emissions from Global Ozone Monitoring Experiment satellite image sequences, Journal of Geophysical Research: Atmospheres, 106, 5493-5505, 10.1029/2000jd900572, 2001.

Levelt, P. F., Zweers, D. C. S., Aben, I., Bauwens, M., Borsdorff, T., De Smedt, I., Eskes, H. J., Lerot, C., Loyola, D. G., Romahn, F., Stavrakou, T., Theys, N., Van Roozendael, M., Veefkind, J. P., and Verhoelst, T.: Air quality impacts of COVID-19 lockdown measures detected from space using high spatial resolution observations of multiple trace gases from Sentinel-5P/TROPOMI, Atmospheric Chemistry and Physics, 22, 10319-10351, 10.5194/acp-22-10319-2022, 2022.

Li, M., McDonald, B. C., McKeen, S. A., Eskes, H., Levelt, P., Francoeur, C., Harkins, C., He, J., Barth, M., Henze, D. K., Bela, M. M., Trainer, M., de Gouw, J. A., and Frost, G. J.: Assessment of Updated Fuel-Based Emissions Inventories Over the Contiguous United States Using TROPOMI NO2 Retrievals, Journal of Geophysical Research-Atmospheres, 126, 10.1029/2021jd035484, 2021.

832   Li, M., Zhang, Q., Kurokawa, J.-i., Woo, J.-H., He, K., Lu, Z., Ohara, T., Song, Y., Streets, D. G.,

833   Carmichael, G. R., Cheng, Y., Hong, C., Huo, H., Jiang, X., Kang, S., Liu, F., Su, H., and Zheng,

834   B.: MIX: a mosaic Asian anthropogenic emission inventory under the international collaboration

835   framework of the MICS-Asia and HTAP, Atmospheric Chemistry and Physics, 17, 935-963,

836   10.5194/acp-17-935-2017, 2017.

837   Liu, F., Page, A., Strode, S. A., Yoshida, Y., Choi, S., Zheng, B., Lamsal, L. N., Li, C., Krotkov,

838   N. A., Eskes, H., van der A, R., Veefkind, P., Levelt, P. F., Hauser, O. P., and Joiner, J.: Abrupt

839   decline in tropospheric nitrogen dioxide over China after the outbreak of COVID-19, Science

840   Advances, 6, 10.1126/sciadv.abc2992, 2020a.

841   Liu, S. C., Trainer, M., Fehsenfeld, F. C., Parrish, D. D., Williams, E. J., Fahey, D. W., Hubler,

842   G., and Murphy, P. C.: Ozone production in the rural troposphere and the implications for regional

843   and global ozone distributions, Journal of Geophysical Research-Atmospheres, 92, 4191-4207,

844   10.1029/JD092iD04p04191, 1987.

845   Liu, T., Wang, X., Hu, J., Wang, Q., An, J., Gong, K., Sun, J., Li, L., Qin, M., Li, J., Tian, J.,

846   Huang, Y., Liao, H., Zhou, M., Hu, Q., Yan, R., Wang, H., and Huang, C.: Driving Forces of

847   Changes in Air Quality during the COVID-19 Lockdown Period in the Yangtze River Delta

848   Region, China, Environmental Science & Technology Letters, 7, 779-786,

849   10.1021/acs.estlett.0c00511, 2020b.

850   Liu, Y. M., Wang, T., Stavrakou, T., Elguindi, N., Doumbia, T., Granier, C., Bouarar, I., Gaubert,

851   B., and Brasseur, G. P.: Diverse response of surface ozone to COVID-19 lockdown in China,

852   Science of the Total Environment, 789, 10.1016/j.scitotenv.2021.147739, 2021.

853   Lu, X., Zhang, L., Chen, Y. F., Zhou, M., Zheng, B., Li, K., Liu, Y. M., Lin, J. T., Fu, T. M., and

854   Zhang, Q.: Exploring 2016-2017 surface ozone pollution over China: source contributions and

855   meteorological influences, Atmospheric Chemistry and Physics, 19, 8339-8361, 10.5194/acp-19-

856   8339-2019, 2019.

857   Mao, J., Paulot, F., Jacob, D. J., Cohen, R. C., Crounse, J. D., Wennberg, P. O., Keller, C. A.,

858   Hudman, R. C., Barkley, M. P., and Horowitz, L. W.: Ozone and organic nitrates over the eastern

859   United States: Sensitivity to isoprene chemistry, Journal of Geophysical Research: Atmospheres,

860   118, 11,256-211,268, 10.1002/jgrd.50817, 2013.

861   Mao, J., Jacob, D. J., Evans, M. J., Olson, J. R., Ren, X., Brune, W. H., Clair, J. M. S., Crounse, J.

862   D., Spencer, K. M., Beaver, M. R., Wennberg, P. O., Cubison, M. J., Jimenez, J. L., Fried, A.,

863 Weibring, P., Walega, J. G., Hall, S. R., Weinheimer, A. J., Cohen, R. C., Chen, G., Crawford, J.

864 H., McNaughton, C., Clarke, A. D., Jaeglé, L., Fisher, J. A., Yantosca, R. M., Le Sager, P., and

865 Carouge, C.: Chemistry of hydrogen oxide radicals (HOx) in the Arctic troposphere in spring,

866 Atmospheric Chemistry and Physics, 10, 5823-5838, 10.5194/acp-10-5823-2010, 2010.

867 Martin, R. V., Jacob, D. J., Chance, K., Kurosu, T. P., Palmer, P. I., and Evans, M. J.: Global

868 inventory of nitrogen oxide emissions constrained by space-based observations of NO2 columns,

869 Journal of Geophysical Research-Atmospheres, 108, 10.1029/2003jd003453, 2003.

870 Miyazaki, K., Bowman, K., Sekiya, T., Jiang, Z., Chen, X., Eskes, H., Ru, M., Zhang, Y., and

871 Shindell, D.: Air Quality Response in China Linked to the 2019 Novel Coronavirus (COVID-19)

872 Lockdown, Geophys Res Lett, 47, 10.1029/2020gl089252, 2020.

873 Murray, L. T., Jacob, D. J., Logan, J. A., Hudman, R. C., and Koshak, W. J.: Optimized regional

874 and interannual variability of lightning in a global chemical transport model constrained by

875 LIS/OTD satellite data, Journal of Geophysical Research: Atmospheres, 117,

876 10.1029/2012jd017934, 2012.

877 Ott, L. E., Pickering, K. E., Stenchikov, G. L., Allen, D. J., DeCaria, A. J., Ridley, B., Lin, R.-F.,

878 Lang, S., and Tao, W.-K.: Production of lightning NOx and its vertical distribution calculated from

879 three-dimensional cloud-scale chemical transport model simulations, Journal of Geophysical

880 Research, 115, 10.1029/2009jd011880, 2010.

881 Palmer, P. I., Jacob, D. J., Chance, K., Martin, R. V., Spurr, R. J. D., Kurosu, T. P., Bey, I.,

882 Yantosca, R., Fiore, A., and Li, Q. B.: Air mass factor formulation for spectroscopic measurements

883 from satellites: Application to formaldehyde retrievals from the Global Ozone Monitoring

884 Experiment, Journal of Geophysical Research-Atmospheres, 106, 14539-14550,

885 10.1029/2000jd900772, 2001.

886 Pusede, S. E., Steiner, A. L., and Cohen, R. C.: Temperature and Recent Trends in the Chemistry

887 of Continental Surface Ozone, Chemical Reviews, 115, 3898-3918, 10.1021/cr5006815, 2015.

888 Qu, Z., Henze, D. K., Capps, S. L., Wang, Y., Xu, X., Wang, J., and Keller, M.: Monthly top-down

889 NOx emissions for China (2005–2012): A hybrid inversion method and trend analysis, Journal of

890 Geophysical Research: Atmospheres, 122, 4600-4625, 10.1002/2016JD025852, 2017.

891 Qu, Z., Henze, D. K., Li, C., Theys, N., Wang, Y., Wang, J., Wang, W., Han, J., Shim, C.,

892 Dickerson, R. R., and Ren, X.: SO2 Emission Estimates Using OMI SO2 Retrievals for 2005-2017,

893 J Geophys Res Atmos, 124, 8336-8359, 10.1029/2019JD030243, 2019.

894 Sha, T., Ma, X. Y., Zhang, H. X., Janechek, N., Wang, Y. Y., Wang, Y., Garcia, L. C., Jenerette,
895 G. D., and Wang, J.: Impacts of Soil NOx Emission on O-3 Air Quality in Rural California,
896 Environmental Science & Technology, 55, 7113-7122, 10.1021/acs.est.0c06834, 2021.

897 Shi, X. and Brasseur, G. P.: The Response in Air Quality to the Reduction of Chinese Economic
898 Activities During the COVID‐19 Outbreak, Geophys Res Lett, 47, 10.1029/2020gl088070, 2020.

899 Sillman, S., Logan, J. A., and Wofsy, S. C.: The sensitivity of ozone to nitrogen-oxides and
900 hydrocarbons in regional ozone episodes, Journal of Geophysical Research-Atmospheres, 95,
901 1837-1851, 10.1029/JD095iD02p01837, 1990.

902 Steinbacher, M., Zellweger, C., Schwarzenbach, B., Bugmann, S., Buchmann, B., Ordóñez, C.,
903 Prevot, A. S. H., and Hueglin, C.: Nitrogen oxide measurements at rural sites in Switzerland: Bias
904 of conventional measurement techniques, Journal of Geophysical Research: Atmospheres, 112,
905 https://doi.org/10.1029/2006JD007971, 2007.

906 Streets, D. G., Canty, T., Carmichael, G. R., de Foy, B., Dickerson, R. R., Duncan, B. N., Edwards,
907 D. P., Haynes, J. A., Henze, D. K., Houyoux, M. R., Jacob, D. J., Krotkov, N. A., Lamsal, L. N.,
908 Liu, Y., Lu, Z., Martin, R. V., Pfister, G. G., Pinder, R. W., Salawitch, R. J., and Wecht, K. J.:
909 Emissions estimation from satellite retrievals: A review of current capability, Atmospheric
910 Environment, 77, 1011-1042, 10.1016/j.atmosenv.2013.05.051, 2013.

911 Sun, K., Zhu, L., Cady-Pereira, K., Chan Miller, C., Chance, K., Clarisse, L., Coheur, P.-F.,
912 González Abad, G., Huang, G., Liu, X., Van Damme, M., Yang, K., and Zondlo, M.: A physics-
913 based approach to oversample multi-satellite, multispecies observations to a common grid,
914 Atmospheric Measurement Techniques, 11, 6679-6701, 10.5194/amt-11-6679-2018, 2018.

915 Tong, L., Liu, Y., Meng, Y., Dai, X. R., Huang, L. J., Luo, W. X., Yang, M. R., Pan, Y., Zheng,
916 J., and Xiao, H.: Surface ozone changes during the COVID-19 outbreak in China: An insight into
917 the pollution characteristics and formation regimes of ozone in the cold season, Journal of
918 Atmospheric Chemistry, 80, 103-120, 10.1007/s10874-022-09443-2, 2023.

919 Travis, K. R., Jacob, D. J., Keller, C. A., Kuang, S., Lin, J., Newchurch, M. J., and Thompson, A.
920 M.: Resolving ozone vertical gradients in air quality models, Atmos. Chem. Phys. Discuss., 2017,
921 1-18, 10.5194/acp-2017-596, 2017.

922 Travis, K. R., Jacob, D. J., Fisher, J. A., Kim, P. S., Marais, E. A., Zhu, L., Yu, K., Miller, C. C.,
923 Yantosca, R. M., Sulprizio, M. P., Thompson, A. M., Wennberg, P. O., Crounse, J. D., St Clair, J.
924 M., Cohen, R. C., Laughner, J. L., Dibb, J. E., Hall, S. R., Ullmann, K., Wolfe, G. M., Pollack, I.

925   B., Peischl, J., Neuman, J. A., and Zhou, X.: Why do Models Overestimate Surface Ozone in the

926   Southeastern United States?, Atmos Chem Phys, 16, 13561-13577, 10.5194/acp-16-13561-2016,

927   2016.

928   van der Werf, G. R., Randerson, J. T., Giglio, L., van Leeuwen, T. T., Chen, Y., Rogers, B. M.,

929   Mu, M., van Marle, M. J. E., Morton, D. C., Collatz, G. J., Yokelson, R. J., and Kasibhatla, P. S.:

930   Global fire emissions estimates during 1997–2016, Earth System Science Data, 9, 697-720,

931   10.5194/essd-9-697-2017, 2017.

932   TROPOMI   ATBD   of   the   total   and   tropospheric   NO2   data   products:

933   https://sentinel.esa.int/documents/247904/2476257/sentinel-5p-tropomi-atbd-no2-data-products,

934   last access: Sep. 29.

935   van Geffen, J., Boersma, K. F., Eskes, H., Sneep, M., ter Linden, M., Zara, M., and Veefkind, J.

936   P.: S5P TROPOMI NO2 slant column retrieval: method, stability, uncertainties and comparisons

937   with OMI, Atmospheric Measurement Techniques, 13, 1315-1335, 10.5194/amt-13-1315-2020,

938   2020.

939   Veefkind, J. P., Aben, I., McMullan, K., Förster, H., de Vries, J., Otter, G., Claas, J., Eskes, H. J.,

940   de Haan, J. F., Kleipool, Q., van Weele, M., Hasekamp, O., Hoogeveen, R., Landgraf, J., Snel, R.,

941   Tol, P., Ingmann, P., Voors, R., Kruizinga, B., Vink, R., Visser, H., and Levelt, P. F.: TROPOMI

942   on the ESA Sentinel-5 Precursor: A GMES mission for global observations of the atmospheric

943   composition for climate, air quality and ozone layer applications, Remote Sensing of Environment,

944   120, 70-83, https://doi.org/10.1016/j.rse.2011.09.027, 2012.

945   Venter, Z. S., Aunan, K., Chowdhury, S., and Lelieveld, J.: COVID-19 lockdowns cause global

946   air pollution declines, Proceedings of the National Academy of Sciences, 117, 18984-18990,

947   doi:10.1073/pnas.2006853117, 2020.

948   Verhoelst, T., Compernolle, S., Pinardi, G., Lambert, J. C., Eskes, H. J., Eichmann, K. U., Fjæraa,

949   A. M., Granville, J., Niemeijer, S., Cede, A., Tiefengraber, M., Hendrick, F., Pazmiño, A., Bais,

950   A., Bazureau, A., Boersma, K. F., Bognar, K., Dehn, A., Donner, S., Elokhov, A., Gebetsberger,

951   M., Goutail, F., de la Mora, M. G., Gruzdev, A., Gratsea, M., Hansen, G. H., Irie, H., Jepsen, N.,

952   Kanaya, Y., Karagkiozidis, D., Kivi, R., Kreher, K., Levelt, P. F., Liu, C., Müller, M., Comas, M.

953   N., Piters, A. J. M., Pommereau, J. P., Portafaix, T., Prados-Roman, C., Puentedura, O., Querel,

954   R., Remmers, J., Richter, A., Rimmer, J., Cárdenas, C. R., de Miguel, L. S., Sinyakov, V. P.,

955   Stremme, W., Strong, K., Van Roozendael, M., Veefkind, J. P., Wagner, T., Wittrock, F., González,

956 M. Y., and Zehner, C.: Ground-based validation of the Copernicus Sentinel-5P TROPOMI NO2
957 measurements with the NDACC ZSL-DOAS, MAX-DOAS and Pandonia global networks,
958 Atmospheric Measurement Techniques, 14, 481-510, 10.5194/amt-14-481-2021, 2021.

959 Vigouroux, C., Langerock, B., Aquino, C. A. B., Blumenstock, T., Cheng, Z. B., De Mazière, M.,
960 De Smedt, I., Grutter, M., Hannigan, J. W., Jones, N., Kivi, R., Loyola, D., Lutsch, E., Mahieu, E.,
961 Makarova, M., Metzger, J. M., Morino, I., Murata, I., Nagahama, T., Notholt, J., Ortega, I., Palm,
962 M., Pinardi, G., Röhling, A., Smale, D., Stremme, W., Strong, K., Sussmann, R., Té, Y., van
963 Roozendael, M., Wang, P. C., and Winkler, H.: TROPOMI-Sentinel-5 Precursor formaldehyde
964 validation using an extensive network of ground-based Fourier-transform infrared stations,
965 Atmospheric Measurement Techniques, 13, 3751-3767, 10.5194/amt-13-3751-2020, 2020.

966 Vinken, G. C. M., Boersma, K. F., van Donkelaar, A., and Zhang, L.: Constraints on ship NOx
967 emissions in Europe using GEOS-Chem and OMI satellite NO2 observations, Atmos. Chem. Phys.,
968 14, 1353-1369, 10.5194/acp-14-1353-2014, 2014.

969 Wang, H. L., Huang, C., Tao, W., Gao, Y. Q., Wang, S. W., Jing, S. A., Wang, W. J., Yan, R. S.,
970 Wang, Q., An, J. Y., Tian, J. J., Hu, Q. Y., Lou, S. R., Pöschl, U., Cheng, Y. F., and Su, H.:
971 Seasonality and reduced nitric oxide titration dominated ozone increase during COVID-19
972 lockdown in eastern China, Npj Climate and Atmospheric Science, 5, 10.1038/s41612-022-00249-
973 3, 2022.

974 Wang, Y., Wang, J., Xu, X., Henze, D. K., Qu, Z., and Yang, K.: Inverse modeling of SO_2 and
975 NO_x emissions over China using multisensor satellite data – Part 1: Formulation and sensitivity
976 analysis, Atmospheric Chemistry and Physics, 20, 6631-6650, 10.5194/acp-20-6631-2020, 2020a.

977 Wang, Y., Wang, J., Zhou, M., Henze, D. K., Ge, C., and Wang, W.: Inverse modeling of SO_2 and
978 NO_x emissions over China using multisensor satellite data – Part 2: Downscaling techniques for
979 air quality analysis and forecasts, Atmospheric Chemistry and Physics, 20, 6651-6670,
980 10.5194/acp-20-6651-2020, 2020b.

981 Wang, Y. X., McElroy, M. B., Jacob, D. J., and Yantosca, R. M.: A nested grid formulation for
982 chemical transport over Asia: Applications to CO, Journal of Geophysical Research: Atmospheres,
983 109, n/a-n/a, 10.1029/2004jd005237, 2004.

984 Williams, J. and Koppmann, R.: Volatile Organic Compounds in the Atmosphere: An Overview,
985 in: Volatile Organic Compounds in the Atmosphere, 1-32,
986 https://doi.org/10.1002/9780470988657.ch1, 2007.

987   Zhang, L., Jacob, D. J., Knipping, E. M., Kumar, N., Munger, J. W., Carouge, C. C., van Donkelaar,
988   A., Wang, Y. X., and Chen, D.: Nitrogen deposition to the United States: distribution, sources, and
989   processes, Atmospheric Chemistry and Physics, 12, 4539-4554, 10.5194/acp-12-4539-2012, 2012.

990   Zhang, Q., Pan, Y., He, Y., Walters, W. W., Ni, Q., Liu, X., Xu, G., Shao, J., and Jiang, C.:
991   Substantial nitrogen oxides emission reduction from China due to COVID-19 and its impact on
992   surface ozone and aerosol pollution, Science of The Total Environment, 753,
993   10.1016/j.scitotenv.2020.142238, 2021.

994   Zhang, R. X., Zhang, Y. Z., Lin, H. P., Feng, X., Fu, T. M., and Wang, Y. H.: NOx Emission
995   Reduction and Recovery during COVID-19 in East China, Atmosphere, 11,
996   10.3390/atmos11040433, 2020.

997   Zhang, Y.-L. and Cao, F.: Fine particulate matter (PM2.5) in China at a city level, Scientific
998   Reports, 5, 14884, 10.1038/srep14884, 2015.

999   Zhao, Y., Zhang, K., Xu, X., Shen, H., Zhu, X., Zhang, Y., Hu, Y., and Shen, G.: Substantial
1000   Changes in Nitrogen Dioxide and Ozone after Excluding Meteorological Impacts during the
1001   COVID-19 Outbreak in Mainland China, Environmental Science & Technology Letters, 7, 402-
1002   408, 10.1021/acs.estlett.0c00304, 2020.

1003   Zheng, B., Tong, D., Li, M., Liu, F., Hong, C., Geng, G., Li, H., Li, X., Peng, L., Qi, J., Yan, L.,
1004   Zhang, Y., Zhao, H., Zheng, Y., He, K., and Zhang, Q.: Trends in China's anthropogenic emissions
1005   since 2010 as the consequence of clean air actions, Atmospheric Chemistry and Physics, 18,
1006   14095-14111, 10.5194/acp-18-14095-2018, 2018.

1007